

# A Series of Iron Nitrosyl Complexes $\{\text{Fe-NO}\}^{6-9}$ and a Fleeting $\{\text{Fe-NO}\}^{10}$ Intermediate en Route to a Metalacyclic Iron Nitrosoalkane

Martin Keilwerth,<sup>†</sup> Johannes Hohenberger,<sup>†</sup> Frank W. Heinemann,<sup>†</sup> Jörg Sutter,<sup>†</sup> Andreas Scheurer,<sup>†</sup> Huayi Fang,<sup>‡,§</sup> Eckhard Bill,<sup>‡</sup> Frank Neese,<sup>§</sup> Shengfa Ye,<sup>\*,§</sup> and Karsten Meyer<sup>\*,†</sup>

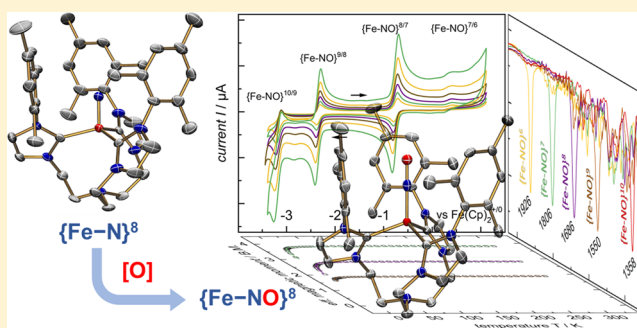
<sup>†</sup>Department of Chemistry and Pharmacy, Inorganic Chemistry, Friedrich-Alexander-University Erlangen-Nürnberg (FAU), Egerlandstrasse 1, D-91058 Erlangen, Germany

<sup>‡</sup>Max-Planck-Institut für Chemische Energiekonversion, Stiftstraße 34-36, D-45470 Mülheim an der Ruhr, Germany

<sup>§</sup>Max-Planck-Institut für Kohlenforschung, Kaiser-Wilhelmplatz 1, D-45470 Mülheim an der Ruhr, Germany

## Supporting Information

**ABSTRACT:** Iron–nitrosyls have fascinated chemists for a long time due to the noninnocent nature of the NO ligand that can exist in up to five different oxidation and spin states. Coordination to an open-shell iron center leads to complex electronic structures, which is the reason Enemark–Feltham introduced the  $\{\text{Fe-NO}\}^n$  notation. In this work, we succeeded in characterizing a series of  $\{\text{Fe-NO}\}^{6-9}$  complexes, including a reactive  $\{\text{Fe-NO}\}^{10}$  intermediate. All complexes were synthesized with the tris-*N*-heterocyclic carbene ligand tris[2-(3-mesitylimidazol-2-ylidene)ethyl]amine (TIMEN<sup>Mes</sup>), which is known to support iron in high and low oxidation states. Reaction of NOBF<sub>4</sub> with  $[(\text{TIMEN}^{\text{Mes}})\text{Fe}]^{2+}$  resulted in formation of the  $\{\text{Fe-NO}\}^6$  compound  $[(\text{TIMEN}^{\text{Mes}})\text{Fe}(\text{NO})(\text{CH}_3\text{CN})](\text{BF}_4)_3$  (**1**). Stepwise chemical reduction with Zn, Mg, and Na/Hg leads to the isostructural series of high-spin iron nitrosyl complexes  $\{\text{Fe-NO}\}^{7,8,9}$  (**2–4**). Reduction of  $\{\text{Fe-NO}\}^9$  with Cs electride finally yields the highly reduced  $\{\text{Fe-NO}\}^{10}$  intermediate, key to formation of  $[\text{Cs}(\text{crypt-222})][(\text{TIMEN}^{\text{Mes}})\text{Fe}(\text{NO})]$ , (**5**) featuring a metalacyclic  $[\text{Fe}-(\text{NO}-\text{NHC})^{3-}]$  nitrosoalkane unit. All complexes were characterized by single-crystal XRD analyses, temperature and field-dependent SQUID magnetization methods, as well as <sup>57</sup>Fe Mössbauer, IR, UV/vis, multinuclear NMR, and dual-mode EPR spectroscopy. Spectroscopy-based DFT analyses provide insight into the electronic structures of all compounds and allowed assignments of oxidation states to iron and NO ligands. An alternative synthesis to the  $\{\text{Fe-NO}\}^8$  complex was found via oxygenation of the nitride complex  $[(\text{TIMEN}^{\text{Mes}})\text{Fe}(\text{N})](\text{BF}_4)$ . Surprisingly, the resulting  $\{\text{Fe-NO}\}^8$  species is electronically and structural similar to the  $[(\text{TIMEN}^{\text{Mes}})\text{Fe}(\text{N})]^+$  precursor. Based on the structural and electronic similarities between this nitrosyl/nitride complex couple, we adopted the strategy, developed by Wieghardt et al., of extending the Enemark–Feltham nomenclature to nitrido complexes, rendering  $[(\text{TIMEN}^{\text{Mes}})\text{Fe}(\text{N})]^+$  as a  $\{\text{Fe-N}\}^8$  species.



## INTRODUCTION

Nitrogen oxide species ( $\text{NO}_x$ ) have long been known to induce physiological effects in living organisms. Among the numerous  $\text{NO}_x$  species, nitric oxide (NO) is especially important with a variety of biochemical functions, ranging from signaling molecule to neurotransmission and immune response, and is also an intermediate within the biogeochemical nitrogen cycle.<sup>1–3</sup> Driven by the importance of iron nitrosyl fleeting intermediates to medicinal and biological chemistry, there is an apparent renaissance of research aimed at elucidating the molecular as well as electronic structure of iron nitrosyl coordination compounds.<sup>4–7</sup> Essential to cellular NO detoxification and reduction of  $\text{NO}_x$  species in the nitrogen cycle are, for instance, heme and nonheme iron-containing enzymes, so-called nitric oxide reductases (NORs) that are performing

the relevant reaction steps in the assimilatory nitrate ( $\text{NO}_3^-$ ) reduction to ammonium ( $\text{NH}_4^+$ ) or the denitrification of  $\text{NO}_3^-$  to dinitrogen ( $\text{N}_2$ ).<sup>8</sup> The latter reduction is sequential and proceeds via nitrite ( $\text{NO}_2^-$ ), nitric oxide (NO), and nitrous oxide ( $\text{N}_2\text{O}$ ) intermediates. Because of the toxicity of potentially released NO, the NO to  $\text{N}_2\text{O}$  transformation has to be fast.<sup>9</sup> The N–N bond formation of the transformation to  $\text{N}_2\text{O}$  is thought to involve a high-spin ferrous iron complex<sup>10</sup>  $\{\text{Fe}-(\text{H})\text{NO}\}^8$  (Enemark–Feltham nomenclature<sup>11</sup>) with either a nitroxyl ( $\text{NO}^-$ ) or the protonated (HNO) bound ligand.<sup>12,13</sup> Model complexes with this reactive  $\{\text{Fe}-(\text{H})\text{NO}\}^8$  moiety are exceedingly rare and, therefore, synthetic routes to

Received: July 27, 2019

Published: September 30, 2019

{Fe–NO}<sup>8</sup> type model complexes and their spectroscopic characterization are especially desirable. The isolation of {Fe–NO}<sup>8</sup>—either by reduction of {Fe–NO}<sup>7</sup> precursors or, alternatively, by oxygenation of an appropriate iron nitride—is challenging due to the enhanced reactivity of the electron-rich {Fe–NO}<sup>8</sup> species. Pioneering work was accomplished by Wieghardt et al. in 2000 with the comprehensive spectroscopic characterization of a series of low-spin {Fe–NO}<sup>n</sup> (*n* = 6, 7, 8) complexes, [(cyclam)Fe(NO)]<sup>2+/+/0</sup>, including the reported crystal structures of the {Fe–NO}<sup>6</sup> and {Fe–NO}<sup>7</sup> octahedral species.<sup>14,15</sup> In 2016, Meyer and co-workers presented a similar series of {Fe–NO}<sup>6–8</sup> complexes [(<sup>NHCL</sup>)Fe(NO)]<sup>m+</sup> (*m* = 2, 1) with tetragonal symmetry, imposed by the tetrakis-*N*-heterocyclic carbene (NHC) macrocyclic scaffold.<sup>5</sup> This study included the first reported X-ray crystallographic characterization of an {Fe–NO}<sup>8</sup> species, albeit with a low-spin-configured iron center. In the same year, Peters et al. reported a series of structurally characterized trigonal bipyramidal iron nitrosyl complexes [(TPB)Fe(NO)]<sup>+/0/-</sup> stabilized by the tris(phosphine)borane (TPB) ligand.<sup>6</sup> All complexes of this series, that includes the highly reduced {Fe–NO}<sup>9</sup> and {Fe–NO}<sup>10</sup> species, exhibit linearly coordinated NO ligands, and have been described as containing low-spin iron centers. In 2018, the Lehnert group presented the characterization and reactivity of a series of {Fe–NO}<sup>6–8</sup> complexes with a tripodal *N*-anchored peralkylguanidine ligand, namely [(TMG<sub>3</sub>tren)Fe(NO)]<sup>m+</sup> (*m* = 3, 2, 1). These complexes exhibit unusual high-spin ground states with total spin *S* = 1, 3/2, 1, respectively, that are rarely seen for NO complexes. The rare high spin {Fe–NO}<sup>8</sup> species (*S* = 1) was isolable in this case. All complexes were thoroughly characterized, including EXAFS analysis; thus, providing structural information for the high-spin {Fe–NO}<sup>8</sup> complex that was lacking single-crystal X-ray diffraction data.<sup>4</sup> Most recently, Fujisawa, Lehnert, and co-workers communicated the synthesis, structural analysis, and reactivity of an {Fe–NO}<sup>8</sup> species, stabilized in the ligand environment of a sterically encumbered hydrotris(pyrazolyl)borate, [(Tp)Fe(NO)]<sup>3+</sup>, with Tp = potassium hydrotris(3-*tert*-butyl-5-isopropyl-1-pyrazolyl)borate.<sup>16</sup>

In this work, we present the synthesis of an entirely new family of five iron nitrosyl complexes, [(TIMEN<sup>Mes</sup>)Fe(NO)]<sup>m</sup> (*m* = 3+, 2+, 1+, 0, 1-). This series was accomplished by reaction of the coordinatively unsaturated, ferrous complex [(TIMEN<sup>Mes</sup>)Fe]<sup>2+</sup> with NOBF<sub>4</sub> to yield [(TIMEN<sup>Mes</sup>)Fe(NO)(CH<sub>3</sub>CN)]<sup>3+</sup>, {Fe–NO}<sup>6</sup>. Subsequent reduction<sup>17</sup> of this {Fe–NO}<sup>6</sup> complex with stoichiometric amounts of Zn, Mg, Na/Hg, and, finally, the electride [Cs(crypt-222)]<sup>⊖</sup>e<sup>-</sup>,<sup>18–20</sup> resulted in the isolation of a series of complexes {Fe–NO}<sup>6–9</sup> and a nitrosoalkane derivative. Thus, employing the *N*-anchored tris-*N*-heterocyclic carbene chelate TIMEN<sup>Mes</sup>,<sup>21</sup> we succeeded in synthesizing the most complete series of iron nitrosyl complexes ever isolated and characterized to date. This pentade of iron nitrosyl species also includes the fully characterized [(TIMEN<sup>Mes</sup>)Fe(NO)]BF<sub>4</sub>; providing one of the first examples<sup>16</sup> of an X-ray crystallographically characterized high-spin {Fe–NO}<sup>8</sup> complex.

Notably, an alternative synthetic route to the rare {Fe–NO}<sup>8</sup> species was established via oxygenation of the corresponding Fe(IV) nitride, [(TIMEN<sup>Mes</sup>)Fe(N)]<sup>+</sup>. This route of transformation<sup>22</sup> is not unprecedented but astonishing nonetheless, considering that in this reaction an oxygen-atom transfer to a high-valent metal nitrido complex leads to the formation of a formally low-valent metal nitrosyl species. In

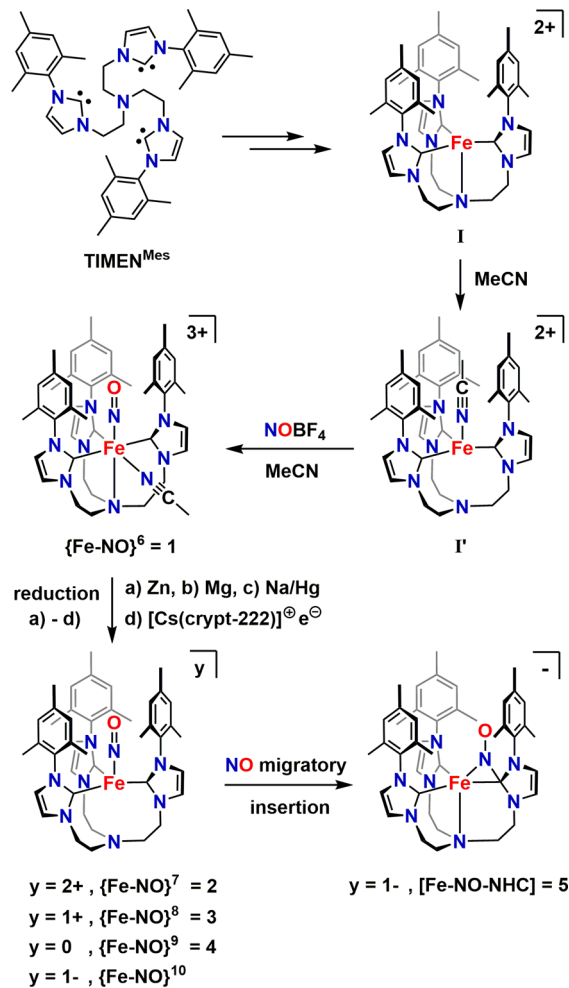
order to further elucidate this remarkable “reduction” by, formally, addition of atomic oxygen [O], we studied the two species [(TIMEN<sup>Mes</sup>)Fe(N)]<sup>+</sup> and [(TIMEN<sup>Mes</sup>)Fe(NO)]<sup>+</sup> in more detail to find that they are electronically and structurally similar.

## RESULTS AND DISCUSSION

**Synthesis and Characterization of the {Fe–NO}<sup>6</sup> Precursor Complex.** All complexes described herein (Scheme 1) are based on the ferrous, coordinatively unsaturated [(TIMEN<sup>Mes</sup>)Fe<sup>II</sup>](BF<sub>4</sub>)<sub>2</sub> starting complex (I) that reacts with nitrosium tetrafluoroborate (NOBF<sub>4</sub>), the source of the nitrogen monoxide (NO) ligand in all complexes. Reaction of I with NOBF<sub>4</sub> in acetonitrile yields [(TIMEN<sup>Mes</sup>)Fe(NO)(CH<sub>3</sub>CN)](BF<sub>4</sub>)<sub>3</sub> (I'), the highest oxidized iron nitrosyl species in the series. According to the Enemark–Feltham nomenclature<sup>11</sup> this complex is referred to as a {Fe–NO}<sup>6</sup> species.

**Crystallographic Data of {Fe–NO}<sup>6</sup>.** Pale-yellow single crystals of complex I, suitable for a single crystal X-ray diffraction study (SC-XRD), were obtained via slow diffusion of Et<sub>2</sub>O into an acetonitrile solution of I at –35 °C. The

**Scheme 1.** Synthesis of [(TIMEN<sup>Mes</sup>)Fe](BF<sub>4</sub>)<sub>2</sub> (I), Its CH<sub>3</sub>CN Adduct (I'), and the Iron Nitrosyl Complexes 1–5



<sup>a</sup>Reaction of I/I' with NOBF<sub>4</sub> forming {Fe–NO}<sup>6</sup> (I) and subsequent reduction leads to the {Fe–NO}<sup>7–10</sup> complexes (2–5).

geometry of the Fe center's first coordination sphere is best described as a  $C_3$ -symmetric, distorted octahedron (Figures 1 and S26). The six-coordinate Fe center is located above the tris-carbene/acetonitrile plane with a  $d_{\text{oop}}$  of 0.017(2) Å, with  $d_{\text{oop}}$  defined as the distance between the Fe center and the plane given by the three NHC carbene carbon atoms and the coordinated acetonitrile nitrogen atom (N9). The average Fe–C<sub>NHC</sub> and Fe–N9 distances are 2.049 and 2.000(2) Å, respectively, with the shortest Fe–C8 bond distance of 2.019(3) Å *trans* to the CH<sub>3</sub>CN ligand. The NO ligand is coordinated in a nearly linear fashion with an  $\angle(\text{Fe–N–O})$  angle of 175.7(2)°. The Fe–N<sub>NO</sub> distance of the NO ligand *trans* to the chelate's amine anchor is 1.654(2) Å, and the N–O bond length is 1.139(3) Å. The distance of the iron center to the anchoring amine N atom is  $d(\text{Fe–N1}) = 2.151(2)$  Å.

**NMR Spectroscopy of {Fe–NO}<sup>6</sup>.** The <sup>1</sup>H NMR spectrum of **1** (400 MHz, Figure 2), recorded in acetonitrile-*d*<sub>3</sub> at 22 °C, exclusively features signals in the diamagnetic chemical shift range, suggesting a nonmagnetic ground state ( $S = 0$ ) of **1** in solution. In contrast to the nonmagnetic,  $C_3$ -symmetric iron nitrido counterpart [(TIMEN<sup>Mes</sup>)Fe(N)]-(BPh)<sub>4</sub> (Fe<sup>IV</sup>,  $d^4$ ,  $S = 0$ ),<sup>23</sup> the spectrum of complex **1**, possessing a  $C_3$  symmetry in the solid state, shows the expected multiple sets of resonances for each proton type. Overall, the spectrum is highly reminiscent of the  $C_3$ -symmetric and diamagnetic manganese nitrido complex [(TIMEN<sup>Xyl</sup>)Mn(N)-(CH<sub>3</sub>CN)](PF<sub>6</sub>)<sub>2</sub> (Mn<sup>V</sup>,  $d^2$ ,  $S = 0$ ),<sup>24</sup> exhibiting an overall similar number and appearance of signals. This observation gave the initial indication that **1**—like its Mn nitrido congener—also exhibits an equatorially coordinated acetonitrile molecule; thus, lacking axial symmetry commonly found for complexes of the TIMEN<sup>R</sup> ligand system. In the spectrum of **1**, each of the nine methyl groups of the TIMEN<sup>Mes</sup> ligand were unambiguously identified by integration and appear as sharp singlets in the diamagnetic range between 2.33 and 1.1 ppm (Figure 2a). The 12 protons of the ethylene bridges give rise to nine signals (b) between 4.99 and 3.01 ppm, and integration reveals that two of these signals originate from five accidentally isochronous proton resonances. The four-spin system of one of the three ethylene bridges gives rise to the characteristic well-resolved doublets of doublets (established by a combination of <sup>1</sup>H, <sup>1</sup>H–<sup>1</sup>H COSY, <sup>13</sup>C, and <sup>1</sup>H–<sup>13</sup>C HMQC as well as HMBC spectra) (Figure 2b). On the basis of

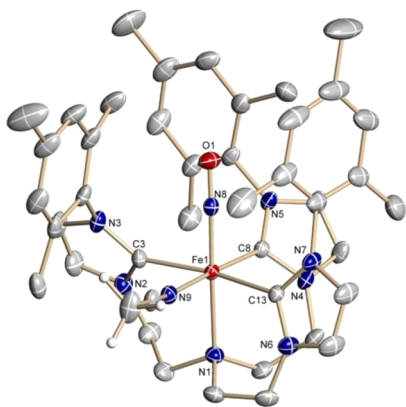


**Figure 1.** Molecular structure of tricationic **1**, {Fe–NO}<sup>6</sup>, in crystals of [(TIMEN<sup>Mes</sup>)Fe(NO)(CH<sub>3</sub>CN)](BF<sub>4</sub>)<sub>3</sub>·2CH<sub>3</sub>CN (50% probability thermal ellipsoids); counterions, hydrogen atoms, except for CH<sub>3</sub>CN, and cocrystallized solvents are omitted for clarity.

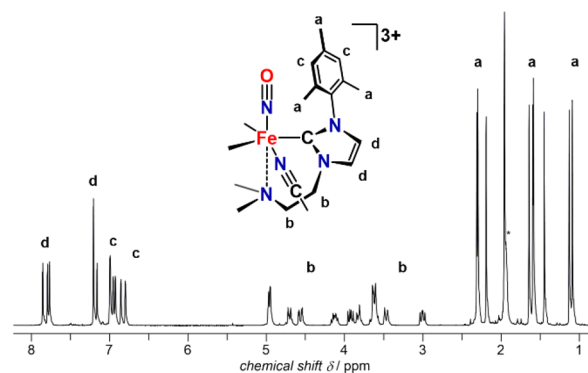


**Figure 2.** <sup>1</sup>H NMR spectrum of **1**, measured at 400 MHz in MeCN-*d*<sub>3</sub> at room temperature. Solvent residual signals are marked with a \*. The two remaining arms of the tripodal NHC-ligand in the molecule depiction are omitted for clarity.

the correlation of the torsion angle  $\Phi$  and vicinal coupling constants (Karplus curve), the spectroscopic data reveal a vicinal coupling constant of  $J \approx 0$  Hz, resulting in  $\Phi$  of around 80–100° in complex **1** in solution.<sup>25–27</sup> In the aromatic region, six singlets (7.01–6.82 ppm) and six doublets (7.86–7.18 ppm) were unequivocally assigned to the protons of the mesityl and imidazol-2-ylidene group, respectively (Figure 2c,d). The  $C_3$  symmetry of **1** was also observed in the <sup>13</sup>C NMR spectrum (101 MHz, CD<sub>3</sub>CN, 22 °C) with each of the 42 carbon atoms of the TIMEN<sup>Mes</sup> ligand producing one signal. Undetected resonances of the carbon atoms are those of the coordinated acetonitrile molecule, likely due to superimposition of the acetonitrile-*d*<sub>3</sub> signals. Notable, the M–C carbene resonances (158.02, 156.36, and 147.53 ppm) are upfield shifted by more than 21 ppm compared to the carbene carbons of the Mn nitrido congener.<sup>24</sup>

**IR Vibrational Spectroscopy of {Fe–NO}<sup>6</sup>.** The IR vibrational spectrum of **1** shows only marginal differences to its precursor **I**, with the most prominent new feature being a sharp, intense absorption band centered at  $\tilde{\nu} = 1926$  cm<sup>-1</sup> (Figure S7). This band is in the characteristic region of the NO stretching vibration of {Fe–NO}<sup>6</sup> complexes and, hence, confirms the coordination of an NO ligand.<sup>4,5,28</sup>

**<sup>57</sup>Fe Mössbauer Spectroscopy of Ferrous Complexes I and I' and of {Fe–NO}<sup>6</sup>.** The coordinatively unsaturated, divalent precursor **I** was characterized by <sup>57</sup>Fe Mössbauer spectroscopy and compared to **1** as well as the structural and spectroscopic fully characterized [(TIMEN<sup>Mes</sup>)Fe(CH<sub>3</sub>CN)]-(BF<sub>4</sub>)<sub>2</sub> acetonitrile adduct (**I'**) (Figure S17).

The zero-field <sup>57</sup>Fe Mössbauer spectra, recorded in the solid state at 77 K, confirm that four-coordinate **I** is closely related to its trigonal bipyramidal acetonitrile adduct **I'**. Both complexes feature single quadrupole doublets with identical isomer shifts,  $\delta$ , of 0.60 mm s<sup>-1</sup>, quadrupole splitting,  $\Delta E_Q$ , of 1.20 mm s<sup>-1</sup> (**I**) and 0.70 mm s<sup>-1</sup> (**I'**), and comparable line widths,  $\Gamma_{\text{fwhm}}$ , of 0.44 mm s<sup>-1</sup>. The parameters are characteristic for high-spin Fe(II) complexes ( $S = 2$ ) within the 3-fold ligand environment of the axial symmetric TIMEN<sup>Mes</sup> chelate; and thus, a similar electronic and molecular structure of both starting materials is suggested.

VT-VF <sup>57</sup>Fe Mössbauer spectra of the {Fe–NO}<sup>6</sup> compound **1** (Figure 3) were measured in the solid state at 80 K in zero magnetic field (top) and at 4.2 and 20 K with fields of 3 and 7 T, respectively (middle and bottom). The weak magnetic splitting observed at 3 and 7 T results solely

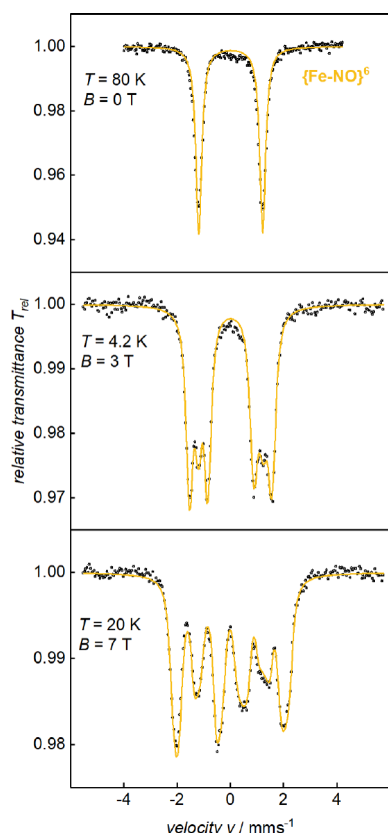


**Figure 3.** Zero and applied-field  $^{57}\text{Fe}$  Mössbauer spectra of **1**, recorded in solid state at 80 K/0 T (top), 4.2 K/3.0 T (middle), and 20 K/7.0 T (bottom). Fields were applied perpendicular to the  $\gamma$ -rays. The yellow lines represent the best global fit obtained for  $S = 0$  with  $\delta = 0.02 \text{ mm s}^{-1}$ ,  $\Delta E_{\text{Q}} = +2.40 \text{ mm s}^{-1}$ ,  $\Gamma_{\text{fwhm}} = 0.26 \text{ mm s}^{-1}$ , and  $\eta = 0.74$ .

from the applied fields, thus, revealing the presence of a diamagnetic ground state,  $S = 0$ . This agrees with the diamagnetism observed in the  $^1\text{H}$  NMR spectrum of **1**. The best global fit of the magnetic Mössbauer spectra was achieved with an isomer shift of  $\delta = 0.02 \text{ mm s}^{-1}$ , a quadrupole splitting  $\Delta E_{\text{Q}} = +2.40 \text{ mm s}^{-1}$ , and importantly, a large asymmetry factor,  $\eta = 0.74$ , of the electric field gradient (EFG). The latter reflects the loss of axial  $C_3$  symmetry already observed in the molecular structure and solution NMR (Figure 2) of **1**, corroborating the equatorially bound  $\text{CH}_3\text{CN}$  after nitrosylation.

The isomer shift and quadrupole splitting of **1** differ significantly from those of ferrous high-spin **I** and **I'**. In particular, the small isomer shift is not consistent with a ferrous or ferric high-spin configuration but is commonly observed for overall low-spin ( $S = 0$ ) iron(II) compounds. The following results of the DFT calculations clearly demonstrate that the  $\{\text{Fe}-\text{NO}\}^6$  complex **1**, in fact, is best described as a low-spin iron(II)  $d^6$  center with a coordinated  $\text{NO}^+$  ligand.

**DFT Calculations of  $\{\text{Fe}-\text{NO}\}^6$ .** To gain more insight into the electronic structure of **1**, we performed detailed DFT calculations on its  $S = 0$  ground state. We tested different closed-shell and broken-symmetry calculations, but all attempts to find broken-symmetry solutions eventually converged to the same closed-shell solution. In particular, the open-shell singlet state corresponding to a low-spin ferric center that is antiferromagnetically coupled to an  $\text{NO}^\bullet$  radical does not

exist in the present case. Specifically, the geometry obtained by restricted closed-shell singlet computations at the B3LYP/def2-TZVP level of theory reproduced the same key metric parameters (Table S3) as determined by single-crystal X-ray diffraction analysis. Notably, the calculations provided the  $^{57}\text{Fe}$  Mössbauer parameters  $\delta = 0.00 \text{ mm s}^{-1}$ ,  $\Delta E_{\text{Q}} = +2.50 \text{ mm s}^{-1}$ , and  $\eta = 0.66$  as well as  $\tilde{\nu}_{\text{NO}} = 1951 \text{ cm}^{-1}$  for the NO stretching band of the IR vibrational spectrum, all in excellent agreement with the experimental data, hence, lending credence to the proposed solution and electronic structure discussed below. The upper valence region of the calculated MO diagram of **1** (Figures 4 and S34), comprises two unoccupied NO  $\pi^*$ -based orbitals. Additionally, one can identify five Fe 3d centered orbitals with the  $t_{2g}$  subshell doubly occupied and the  $e_g$  orbitals vacant. The molecular orbitals (MOs) labeled as Fe  $3d_{xz}$  and Fe  $3d_{yz}$  represent  $\pi$  bonding orbitals with respect to the Fe–NO  $\pi$ -interaction and contain as much as 30% NO  $\pi^*$  character, indicative of strong  $\pi$  backbonding from the iron center to the NO ligand. Hence, the electronic structure of **1** is best described as a low-spin Fe(II)  $d^6$  center, coordinated by an  $\text{NO}^+$  ligand. Noteworthy, the  $S = 0$  spin state in this case is not caused by antiferromagnetic coupling of separated iron and NO-based spin centers, as observed for the reduced  $\{\text{Fe}-\text{NO}\}^{7-9}$  counterparts (vide infra). Remarkably, the electronic structure of **1** is analogous to those found for the [(cyclam-ac)Fe(NO)] $^{2+}$  dication $^{15}$  and the [(TPP)Fe(MI)(NO)] $^+$  complex. $^{29}$  This is interesting, considering how different the coligands are in these compounds.

**Synthesis and Structural Characterization of  $\{\text{Fe}-\text{NO}\}^{7-9}$  Complexes.** Upon reduction with zinc in acetonitrile, the  $\{\text{Fe}-\text{NO}\}^6$  complex **1** releases the equatorially coordinated solvent and forms the green  $\{\text{Fe}-\text{NO}\}^7$  species; namely, [(TIMEN $^{\text{Mes}}$ )Fe(NO)](BF $_4$ ) $_2$  (**2**). Single crystals suitable for an XRD study were obtained via slow *n*-pentane diffusion into a dichloromethane solution of **2** at  $-35^\circ\text{C}$ . Increasing the reaction time and applying magnesium instead of zinc in acetonitrile leads to the formation of the  $\{\text{Fe}-\text{NO}\}^8$  species,

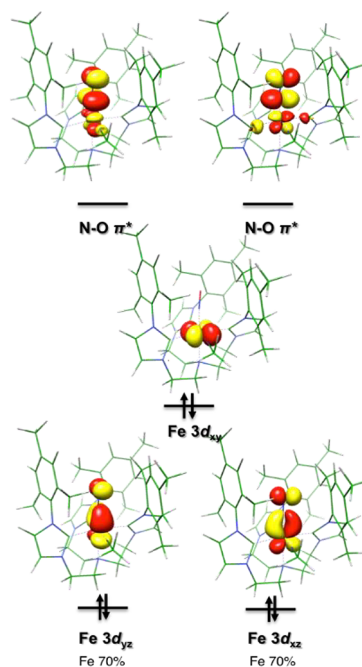


**Figure 4.** Calculated molecular orbital diagram of **1**.

accompanied by a gradual color change from yellow (1) to green (2) to the final purple product  $[(\text{TIMEN}^{\text{Mes}})\text{Fe}(\text{NO})](\text{BF}_4)$  (3). Single crystals of 3 for an XRD study were obtained by slow diffusion of diethyl ether into an acetonitrile solution at  $-35^\circ\text{C}$ . Stored under inert gas atmosphere, 3 shows no sign of decomposition over the course of several weeks; neither in solid state nor in solution. In the solid state, 3 is even stable under aerobic conditions for several days. Green 2 is regenerated, however, after 3 is exposed to air in solution for several hours. This unusual stability of 3 is remarkable for an  $\{\text{Fe}-\text{NO}\}^8$  species.<sup>16,30</sup> Access to even higher reduced forms of the  $[(\text{TIMEN}^{\text{Mes}})\text{Fe}(\text{NO})]^m$  system was achieved by changing the reaction solvent to THF. Reduction of 3 with Na/Hg in THF leads to the formation of the brown  $\{\text{Fe}-\text{NO}\}^9$  complex  $[(\text{TIMEN}^{\text{Mes}})\text{Fe}(\text{NO})]$  (4) that crystallizes by cooling a saturated THF solution to  $-35^\circ\text{C}$ . In  $\text{N}_2$  atmosphere, compound 4 shows no signs of decomposition over several weeks in solution or solid state.

The  $\{\text{Fe}-\text{NO}\}^{7-9}$  complexes 2–4 (Figure 5–7) were obtained in single crystalline form, thus enabling single crystal X-ray diffraction analysis (SC-XRD) and allowing for the structural comparison of the  $\{\text{Fe}-\text{NO}\}^n$  core unit in various oxidation states. The geometry of the core structures can be classified in between trigonal pyramidal and distorted tetrahedral, and it is retained upon consecutive reduction. The  $\{\text{Fe}-\text{NO}\}^7$  complex 2 possesses an out-of-plane shift ( $d_{\text{oop}}$ ) of 0.308(3) Å and an average  $\angle_{\text{av}}(\text{C}-\text{Fe}-\text{N})$  angle of  $98.5^\circ$ , which is slightly closer to the angle expected for a trigonal pyramid ( $90^\circ$ ) than for a tetrahedron ( $109^\circ$ ). The  $\{\text{Fe}-\text{NO}\}^8$  and  $\{\text{Fe}-\text{NO}\}^9$  complexes 3 and 4, on the other hand, are much closer to a tetrahedron, with the iron center located further out of the carbene plane. The  $d_{\text{oop}}$  values range from 0.656(5) to 0.750(5) for the three independent molecules in the unit cell of 3 and amount to 0.642(2) Å in 4, respectively. The average  $\angle_{\text{av}}(\text{C}-\text{Fe}-\text{N})$  angles are almost perfectly tetrahedral with values ranging from  $108.7^\circ$  to  $111.4^\circ$  for the three independent molecules in 3 and  $109.2^\circ$  in 4. Since the observed amine N-to-Fe distances are 2.817(4) Å (2), 3.613 Å (mean value for 3), and 3.594(2) Å (4), respectively, the N-anchor is noncoordinating.

The narrow cylindrical cavity provided by the sterically demanding mesitylene substituents of the  $\text{TIMEN}^{\text{Mes}}$  ligand enforces an almost linear Fe–NO coordination with  $\angle(\text{Fe}-$

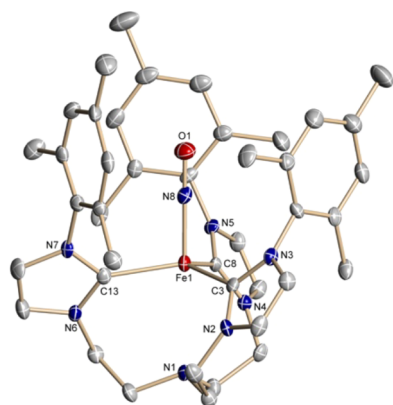


**Figure 5.** Molecular structure of dicationic 2,  $\{\text{Fe}-\text{NO}\}^7$ , in crystals of  $[(\text{TIMEN}^{\text{Mes}})\text{Fe}(\text{NO})](\text{BF}_4)_2 \cdot 3\text{CH}_2\text{Cl}_2$  (50% probability thermal ellipsoids); counterions, hydrogen atoms, and cocrystallized solvents are omitted for clarity.

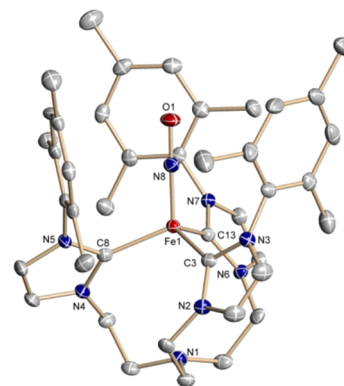


**Figure 6.** Molecular structure of cationic 3,  $\{\text{Fe}-\text{NO}\}^8$ , in crystals of  $[(\text{TIMEN}^{\text{Mes}})\text{Fe}(\text{NO})](\text{BF}_4)$  (50% probability thermal ellipsoids). 3 crystallizes with three independent molecules per unit cell; only one is shown. Counter ions and hydrogen atoms are omitted for clarity.

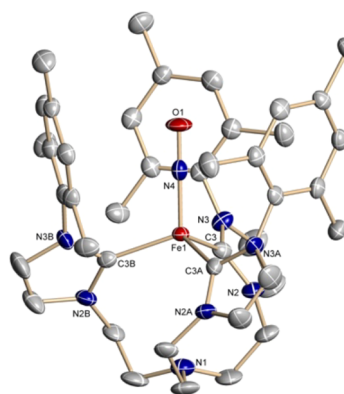


**Figure 7.** Molecular structure of neutral 4,  $\{\text{Fe}-\text{NO}\}^9$ , in crystals of  $[(\text{TIMEN}^{\text{Mes}})\text{Fe}(\text{NO})]$  (50% probability thermal ellipsoids); hydrogen atoms are omitted for clarity.

N–O) angles of  $177.8(4)^\circ$ ,  $180^\circ$ , and  $179.0(2)^\circ$  for 2, 3, and 4 (Table 1); regardless of the NO oxidation state. This linear Fe–NO coordination mode is typically found for complexes with a  $\text{NO}^+$  (nitrosonium) ligand (see  $\{\text{Fe}-\text{NO}\}^6$  complex 1) and often lost upon reduction (and formation of nitroxyl,  $\text{NO}^-$ ).<sup>31–34</sup> Although in case of 3, the Fe–NO unit lies on a crystallographically imposed axis; resulting in an Fe–N–O angle of exactly  $180.00^\circ$ , the overall linear coordination mode seen in 2–4 likely is imposed by the chelate’s cylindrical cavity. Within the triad of  $\{\text{Fe}-\text{NO}\}^{7-9}$  complexes, there are more noteworthy and counterintuitive structural trends that occur upon each reduction. Interestingly, with each reduction step the N–O distance steadily increases, suggesting a decrease in

**Table 1.** Selected Structural Parameters, Bond Lengths (Å), and Angles [ $^\circ$ ] for 2–4

	$\{\text{Fe}-\text{NO}\}^7$ 2	$\{\text{Fe}-\text{NO}\}^8$ 3 <sup>a</sup>	$\{\text{Fe}-\text{NO}\}^9$ 4
space group	<i>Pbca</i>	<i>P3</i>	<i>P2<sub>1</sub>/n</i>
$d_{\text{oop}}$ Fe	0.308(3)	0.701	0.642(2)
$d(\text{Fe}-\text{N})$	1.775(5)	1.681	1.668(3)
$d(\text{N}-\text{O})$	1.149(5)	1.175	1.224(3)
$d(\text{Fe}-\text{C})_{\text{av}}$	2.077	2.051	1.955
$\angle(\text{Fe}-\text{N}-\text{O})$	177.8(4)	180.00	179.0(2)

<sup>a</sup>Complex 3 crystallizes with three independent molecules per unit cell; average values are shown.

N–O bond strength due to higher electron density in the  $\pi^*$  orbitals of the NO ligand (vide infra). Concurrently, the Fe–N and Fe–C distances decrease in the series 2 to 4, supporting evidence for increasing Fe–C<sub>NHC</sub> and Fe–NO  $\pi$  backbonding and simultaneous increase of covalency. These results are rather counterintuitive, as one would expect an increase of metal–ligand bond distances upon reduction. The trends seen in 2–4 are also contrary to the observations made for other reported C<sub>3</sub>-symmetric NO complexes. The series {(TPB)Fe(NO)}<sup>8–10</sup> by Peters et al., for example, exhibits either constant or increasing Fe–NO and Fe–ligand distances.<sup>6,28</sup> The same trend was observed for the series of C<sub>4</sub>-symmetric complexes with the macrocyclic tetra-*N*-heterocyclic carbene ligand {(L<sup>NHC</sup>)Fe(NO)}<sup>6–8</sup>, reported by Meyer et al.<sup>5</sup> The ancillary ligand shows only negligible changes of its bond lengths and angles, implying that the reduction exclusively influences the {Fe–NO}<sup>*n*</sup> core unit.

**Electrochemical Studies of {Fe–NO}<sup>6–10</sup>.** Cyclic voltammetry (CV), linear-sweep, and square-wave measurements (Figures 8, S23, and S24) were conducted in order to determine the exact half-step potential,  $E_{1/2}$ , of each reduction step in the series {Fe–NO}<sup>*n*</sup> ( $n = 6–10$ ). Complexes 1–4 were measured with varying scan rates and solvents, due to the complex stability, with the [Fe(Cp)<sub>2</sub>]<sup>+0</sup> redox pair as an internal standard.

The CV of {Fe–NO}<sup>8</sup> (3), recorded in DMF (Figure 8, top), shows four redox transitions and three reversible one-electron redox-events (Figure S23) at –0.75, –2.35, and –3.16 V as well as one at +0.32 V. While the transition at –3.16 V coincides with the onset of the reductive decomposition of the DMF solvent, the redox transition at +0.32 V appears quasi-

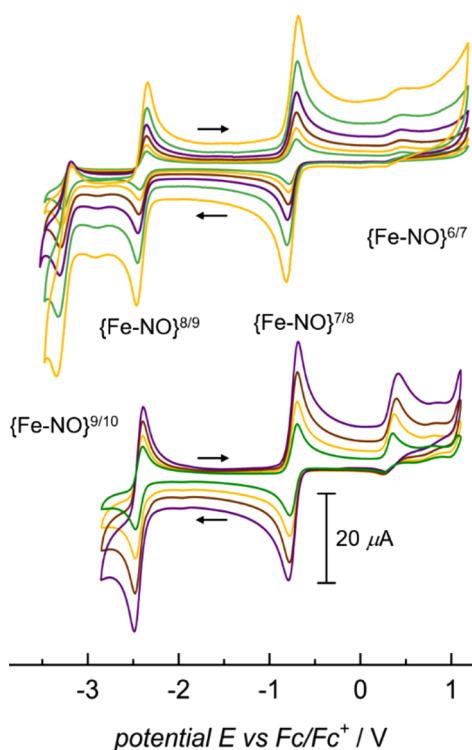


**Figure 8.** Cyclic voltammograms of 3, measured at rt in DMF (top) and MeCN (bottom) solution with 0.1 M N(*n*-Bu)<sub>4</sub>PF<sub>6</sub> electrolyte and varying scan rates (0.05–1.60 V/s), referenced vs Fe(Cp)<sub>2</sub><sup>+/0</sup>/Fe(Cp)<sub>2</sub>.

reversible when studied in acetonitrile solution (Figure 8, bottom). The redox events at negative potentials can be assigned to the {Fe–NO}<sup>7/8</sup>, {Fe–NO}<sup>8/9</sup>, and {Fe–NO}<sup>9/10</sup> redox pairs, respectively. The fourth transition, at  $E_{1/2} = +0.32$  V, can be assigned to the oxidation of 2 to yield the {Fe–NO}<sup>6</sup> complex 1. The weak electrochemical response and quasi-reversibility suggests additional ECE processes upon oxidation. This response is most likely associated with the significant structural (and electronic) changes in the transformation from the octahedral low-spin {Fe–NO}<sup>6</sup> complex 1, with an equatorially coordinated acetonitrile ligand, to the reduced solvent-free, trigonal pyramidal high-spin {Fe–NO}<sup>7</sup> (vide supra); for details regarding the “{Fe–NO}<sup>10</sup>” species 5, see below.

**Spectroscopic and Magnetic Characterization of {Fe–NO}<sup>7–9</sup>.** The consecutive reduction of the {Fe–NO}<sup>6</sup> complex 1, yielding the products 2–5 was closely followed by IR vibrational spectroscopy (Figure 15, vide infra). The wavenumber of the NO stretching band,  $\tilde{\nu}_{\text{NO}}$ , decreases gradually with each reduction step by about 125 cm<sup>–1</sup>, from 1926 (1) to 1806 (2), 1686 (3), and 1550 cm<sup>–1</sup> (4), as shown below in Figure 15. However, it must be emphasized that on the basis of NO stretching frequency shifts alone, one cannot conclude whether the redox processes is metal or NO-centered, since both are frequently accompanied by considerable bathochromic shifts of the NO stretching frequencies.<sup>5</sup>

To explore the electronic structures of the nitrosyl compounds in detail, various spectroscopic techniques were applied. Specifically, magnetic susceptibility measurements at variable temperatures and variable magnetic fields (VT-VF) give insight into the magnetic ground states and zero-field splitting of complexes 2–4 (Figure 9). X-band EPR spectroscopy was applied to probe the anisotropic *g* values and rhombicities of the corresponding spin states (Figure 10), and VT-VF <sup>57</sup>Fe Mössbauer spectroscopy was employed to determine the electric and magnetic hyperfine coupling parameters (Figure 11).

**{Fe–NO}<sup>7</sup>.** The susceptibility measurements of powder samples of 2 revealed a constant effective magnetic moment,  $\mu_{\text{eff}}$  of 3.84  $\mu_{\text{B}}$  in the temperature range from 50 K to room temperature, indicative of a well-isolated  $S = 3/2$  total spin state (spin-only value  $\mu_{\text{eff,s.o.}} = 3.87 \mu_{\text{B}}$ ). The combined effects of field saturation and moderate zero-field splitting of the spin manifold caused the observed decrease of  $\mu_{\text{eff}}(T)$  observable below 50 K (Figure 9, top and bottom). Global simulation of the VT-VF magnetic susceptibility and magnetization data yielded an axial splitting parameter  $D = 5.5(3)$  cm<sup>–1</sup>, negligible rhombicity  $E/D \approx 0$ , and an average *g* value of  $g = 2.0(1)$ .

The X-band EPR spectrum of 2 in frozen acetonitrile solution (6 K) shows an axial signal with effective *g* values  $g'_{x/y} \approx 4$  and  $g'_z = 2.01$  (Figure 10, top). In accordance with the SQUID result of the solid sample, the EPR signal is readily assignable to the  $|m_s = \pm 1/2\rangle$  Kramers doublet of the  $S = 3/2$  manifold. The observed effective *g* values are expected for positive  $D \gg h\nu$ ,  $E/D \approx 0$ . The corresponding spin Hamiltonian simulation with  $D = 5.5$  cm<sup>–1</sup> (taken from the magnetic susceptibility simulations) yielded the rhombicity parameter  $E/D = 0.007(4)$  and electronic intrinsic *g* values 2.017, 2.017, 2.00 (*g*-matrix constrained to be axial). The derivative signal at  $g'_{x/y} \approx 4$  is slightly broadened and skewed toward higher fields, which was successfully simulated by introducing a Gaussian distribution of rhombicity values with half-width  $\sigma(E/D) = 0.01$ . We suggest that structural

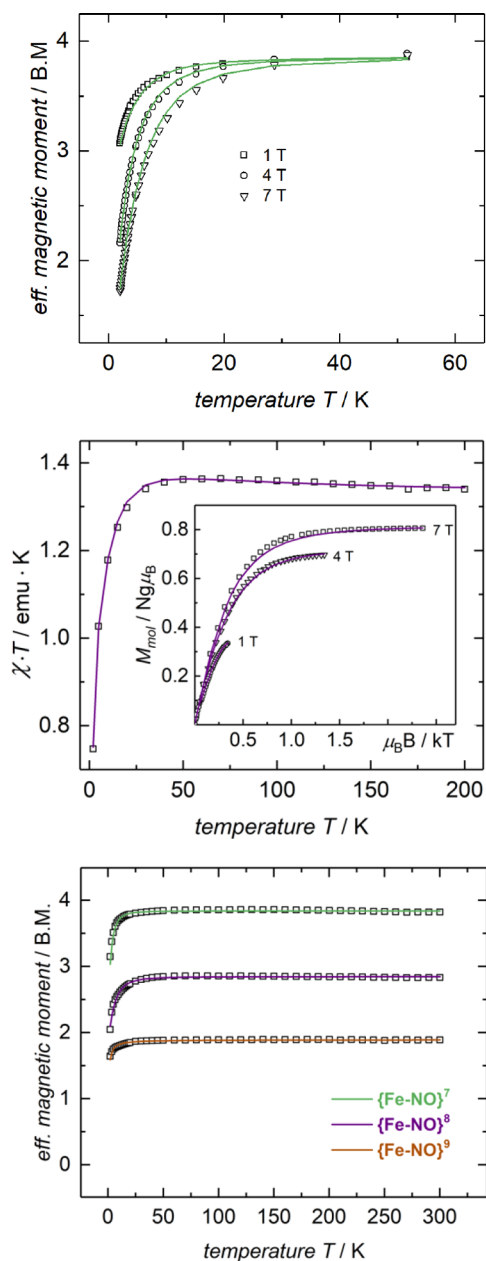


**Figure 9.** VT-VF SQUID magnetization measurements of microcrystalline solid samples of **2** (top, green), **3** (middle, purple), and an overlay of **2–4** recorded at 1 T (bottom). Data reproducibility was tested on independently synthesized and measured samples for each compound. The solid lines represent global fits for  $S = 3/2$  (**2**),  $S = 1$  (**3**), and  $S = 1/2$  (**4**), respectively, with parameters given in the text.

heterogeneity causes the observed perturbation of the axial symmetry of **2** for a fraction of the frozen solution sample.

Solid-state magnetic Mössbauer spectra of complex **2**, recorded at 4.2 K with applied fields of 5 and 7 T perpendicular to the  $\gamma$ -rays, exhibit well-resolved magnetic six-line splitting (Figure 11, left panel bottom, and Figure S19). The overall splitting reveals the presence of a moderately strong internal field  $B_{\text{int}}$  of ca. 24 T ( $B_{\text{int}} = -A\langle S \rangle / g_N \beta_N$ , where  $\langle S \rangle$  is the spin expectation value and  $A$  is the hyperfine coupling matrix). The magnetic six-line spectra of **2** exhibit a clear quadrupole shift as suggested by the relative positions of the outer two lines relative to the inner four lines. The effect results from a weak perturbation of the dominating nuclear

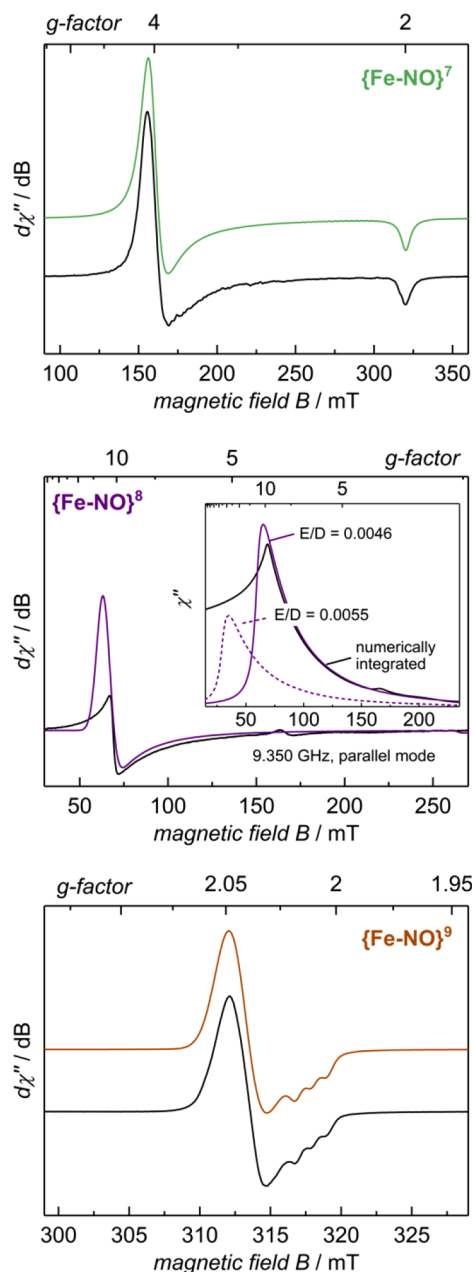


**Figure 10.** X-band EPR spectra of **2** (top, green), **3** (middle, purple), measured at 6 and 3 K in frozen acetonitrile solution, and **4** (bottom, brown), measured at 6 K in dilute frozen THF solution (0.5 mM). The colored lines represent simulations for  $S = 3/2$  (**2**),  $S = 1$  (**3**), and  $S = 1/2$  (**4**), respectively, and with parameters given in Table 2. The inset of the middle panel shows the numerical integration (black trace) of the experimentally determined derivative spectrum of **3** and simulations exhibiting high sensitivity with varying  $E/D$ . The distinct line shape of the absorption (black line) up to zero field, likely reflects some heterogeneity and distribution of  $E/D$ , which could not be resolved in more detail.

Zeeman interaction by weak electric quadrupole interaction and, therefore, depends essentially only on the EFG tensor component along the internal field  $B_{\text{int}}$ . Since the quadrupole shift is well-defined (and not distributed over a range of values, in spite of the powdered sample),  $B_{\text{int}}$  must be well-oriented in the molecular frame; at least at a fixed angle relative to the EFG main  $z$ -axis. Moreover, the relative intensities of the magnetic hyperfine lines, characterized by strong  $\Delta m_l = 0$

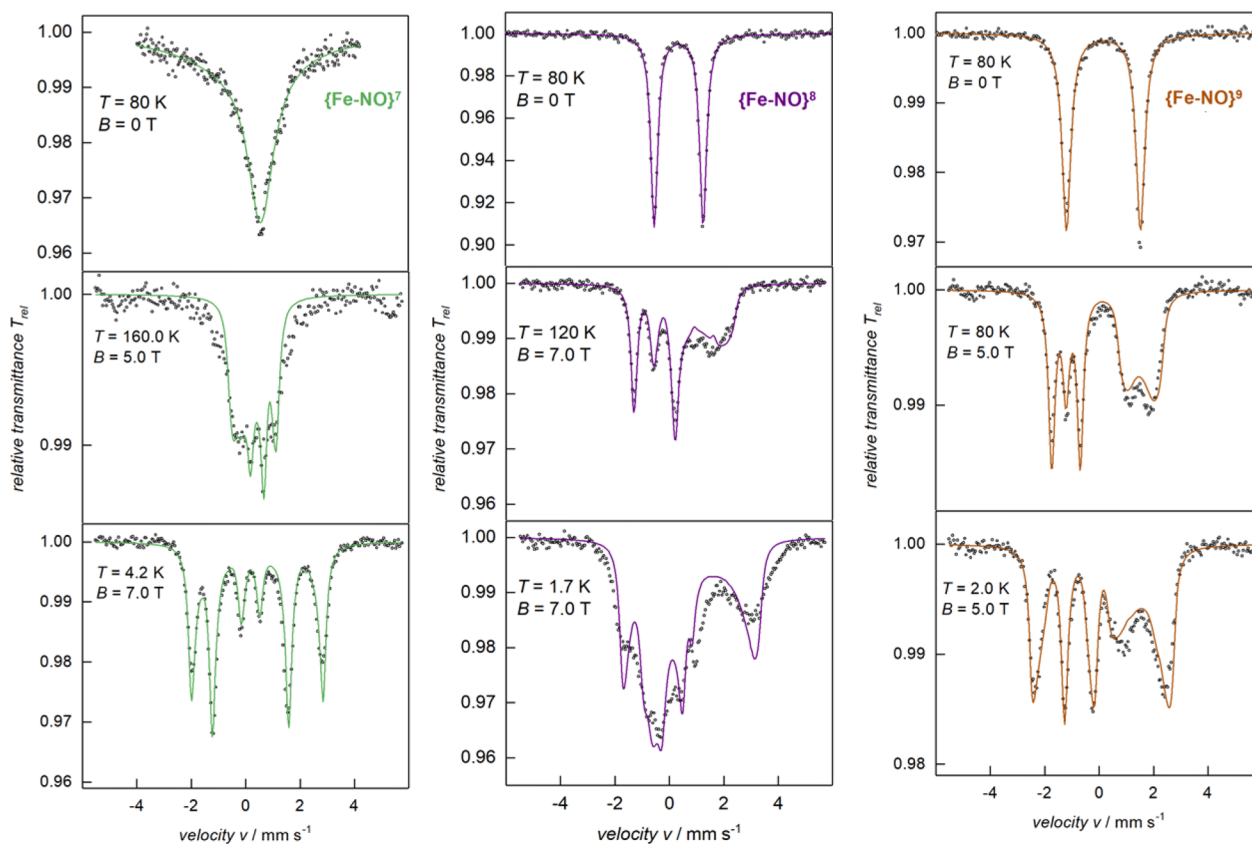


**Figure 11.** VT-VF  $^{57}\text{Fe}$  Mössbauer spectra of  $\{\text{Fe-NO}\}^7$  (2),  $\{\text{Fe-NO}\}^8$  (3), and  $\{\text{Fe-NO}\}^9$  (4), recorded in the solid state. The solid sample of 3 was immobilized by embedding the microcrystals in eicosane ( $\text{C}_{20}\text{H}_{42}$ ). Fields were applied perpendicular to the  $\gamma$ -rays. The colored lines represent the best global fits obtained for the  $S = 3/2$ , 1, and  $1/2$  systems, respectively.

transitions (lines 2 and 5), indicate an easy  $x/y$  plane of magnetization in the ground state of complex 2. This is fully consistent with the positive  $D$  and vanishing  $E/D$  values determined by the SQUID measurements. Because of the easy plane magnetic anisotropy,  $\mathbf{B}_{\text{int}}$  remains preferentially oriented near the molecular  $x/y$  directions throughout the powder sample. Consequently, the observed, distinctly positive quadrupole shift in the spectra reveals positive  $V_{xx}/V_{yy}$  components for the EFG. However, as the EFG is traceless,  $V_{xx} + V_{yy} + V_{zz} = 0$ , the main component  $V_{zz}$  must be negative, and correspondingly, the sign of the quadrupole interaction  $\Delta E_Q$  is also negative for 2.

Well-resolved pure quadrupole spectra of 2 could not be obtained by performing zero-field measurements at elevated temperature (Figure 11, left, top). The lines are broadened due to intermediate relaxation as spin relaxation apparently does not reach the fast limit; neither at 80 nor at 160 K. Nevertheless, because the internal field is weak enough at 160 K with 5 T applied field, the sign of  $\Delta E_Q$  has been confirmed.

Assuming slow relaxation, the low-temperature magnetic Mössbauer spectra of 2 have been satisfactorily simulated with the zero-field splitting parameters taken from SQUID and EPR analyses. The hyperfine coupling matrix  $\mathbf{A}$  was confirmed to be moderately strong and rather isotropic (Table 2). The global simulations gave an isomer shift of  $\delta = 0.31 \text{ mm s}^{-1}$  at 4.2 K, and a weak quadrupole splitting  $\Delta E_Q = -0.51 \text{ mm s}^{-1}$ . The negative sign, as rationalized above, is confirmed by the simulations and the axial symmetry of the EFG, exhibiting a

**Table 2.** Spin Hamiltonian and  $^{57}\text{Fe}$  Mössbauer Parameters of 2–4; Isomer Shift,  $\delta$ , Quadrupole Splitting,  $\Delta E_Q$ , Line Width,  $\Gamma_{\text{fwhm}}$ , All in Units of  $\text{mm s}^{-1}$ , Hyperfine Coupling Constants  $A_{ii}$  (T), and Zero-Field Splitting,  $D$  ( $\text{cm}^{-1}$ )

	$\{\text{Fe-NO}\}^7$ 2	$\{\text{Fe-NO}\}^8$ 3	$\{\text{Fe-NO}\}^9$ 4
$S$	3/2	1	1/2
$\delta$	0.31	0.37	0.17
$\Delta E_Q$	-0.51	1.82	2.73
$\Gamma_{\text{fwhm}}$	0.26	0.26	0.26
$\eta$	0	0	0
$g$ -values	$g_x = 2.02$ $g_y = 2.02$ $g_z = 2.01$	$g_x = 2.02$ $g_y = 2.02$ $g_z = 2.78$	$g_x = 2.03$ $g_y = 2.03$ $g_z = 2.04$
$D$	6	-29	
$E/D$	0	0	
$A_{xx}/g_N\beta_N$	-15.30	-16.50	-31.03
$A_{yy}/g_N\beta_N$	-15.30	-16.50	-31.03
$A_{zz}/g_N\beta_N$	-18.88	9.50	5.26

vanishing asymmetry parameter  $\eta = 0$ , where  $\eta = (V_{xx} + V_{yy})/V_{zz}$ .

$\{\text{Fe-NO}\}^8$ . VT-VF magnetic susceptibility measurements of complex 3 are shown in Figure 9 (middle and bottom panels). The effective magnetic moment  $\mu_{\text{eff}} = 3.28 \mu_B$  at room temperature reveals an overall spin state  $S = 1$  ( $\mu_{\text{eff},\text{s.o.}} = 2.83 \mu_B$ ). The higher than expected moment indicates an average  $g$  value larger than 2.0. A strong temperature decline of  $\mu_{\text{eff}}(T)$  and  $\chi(T) \cdot T$  below 50 K and distinct nesting of iso-field magnetization curves (Figure 9, middle inset) indicate sizable

zero-field splitting of the ground state of **3**. Global simulation of the VT-VF SQUID data revealed an unusually large and negative axial zero-field splitting parameter  $D = -28.9(5)$   $\text{cm}^{-1}$ , negligible rhombicity,  $E/D \approx 0$ , and strong anisotropic  $g$ -values of  $g_x = g_y = 2.02$  and  $g_z = 2.78$  (see also Figures S14 and S15).

Detection of the pronounced  $g$  anisotropy from SQUID powder measurements, as found here for **3**, is rare and only possible if zero-field splitting causes strong magnetic anisotropy of the magnetic sublevels.<sup>35</sup> In our case of  $S = 1$  with large negative  $D$  and  $E/D \approx 0$ , the Zeeman splitting of the low-lying “ $m_s = \pm 1$ ” levels is strong for fields in  $z$  direction but very weak for  $x/y$  directions. Just the opposite behavior is expected for the excited “ $m_s = 0$ ” level. Fields applied along the  $z$ -axis do not affect the nonmagnetic nature and the energy of that level, whereas fields perpendicular to  $z$  mix in  $m_s = \pm 1$  contributions and, thus, induce magnetization (Figure S16). As a consequence, the microscopic magnetization of the “ $m_s = \pm 1$ ” levels preferentially points into the  $z$ -direction for all powder orientations and that of “ $m_s = 0$ ” into the  $x/y$  plane. Furthermore, the magnetization of the powder sample at low temperatures is governed by  $g_z$ , while the influence of the  $g_{x/y}$  values comes into play at elevated temperatures when all  $m_s$  levels are increasingly and uniformly populated. Finally, at high temperatures, the powder average of the  $g$  matrix is determined. Interestingly, the  $\chi \cdot T$  values of **3** with increasing temperatures exhibit a maximum at approximately 50 K before they decline to the high-temperature limit. The behavior is distinctly different from the monotonous increase of  $\chi(T) \cdot T$  or  $\mu_{\text{eff}}(T)$  in the low temperature region without passing through a maximum, commonly observed for mononuclear transition metal complexes, such as **2**, having a weaker zero-field splitting and more isotropic  $g$  values. The overshooting of  $\chi \cdot T$  is unique for **3** and arises solely from the fact that  $g_z$  is much larger than  $g_{x/y}$  (see also Figures S14 and S15).

The  $S = 1$  high-spin state observed here is exceedingly rare for {Fe–NO}<sup>8</sup> complexes, with the only other examples being [(TMG<sub>3</sub>tren)Fe(NO)]<sup>+4,28</sup> and TauD–{Fe–NO}<sup>8</sup> analyzed by some of us.<sup>36</sup> Although VT-VF magnetic data, EPR, and <sup>57</sup>Fe Mössbauer spectroscopic data for [(Tp)Fe(NO)] are not reported, computational analyses of this latest addition of iron nitrosyls to this group of {Fe–NO}<sup>8</sup> species also revealed a ferrous nitroxyl species with an  $S = 1$  ground state, in which the triplet <sup>3</sup>NO<sup>−</sup> ligand is antiferromagnetically coupled to a high-spin Fe(II) ion. The reported magnetic moment (3.13  $\mu_B$ , by the Evans method), the Fe–NO stretch (1696  $\text{cm}^{-1}$ ), and Fe–N–O metric parameters ( $d(\text{Fe–N})$  1.6753(13) Å;  $d(\text{N–O})$  1.1865(17) Å, and  $\angle(\text{Fe–N–O})$ , 176.76(18)<sup>o</sup> of [(Tp)Fe(NO)] are remarkably similar to those of **3**.<sup>16</sup>

Surprisingly, and in spite of its sizable zero-field splitting, the integer-spin complex **3** exhibits intense X-band EPR signals in frozen solution at 3 K (Figure S10). Specifically, a rather sharp signal was observed in *parallel mode* spectra at  $g^* \approx 9$  (Figure 10, middle). The corresponding absorption arises from *quasi*  $\Delta m_s = 2$  transitions between the low-lying “ $m_s = \pm 1$ ” levels of the triplet ground state, which otherwise are forbidden, but only for fields near the molecular  $z$ -direction and  $E/D$  close to zero. The temperature dependence of the EPR signal, being more intense at 3 K than at 10 K, is consistent with the negative  $D$  value derived from the magnetization data of **3**. The resonance condition for the integer-spin EPR transitions of **3**, viz. between the “ $m_s = \pm 1$ ” levels of the  $S = 1$  ground state, is

given by the relation  $\hbar\nu = \sqrt{(2\mu_B g_z B \cos \theta)^2 + \delta_{\pm 1}^2}$ . Here, the angle  $\theta$  describes the orientation of the applied magnetic field relative to the  $z$ -axis of the  $D$  tensor and  $\delta_{\pm 1}$  is the energy separation of the resonance levels without field.<sup>37</sup> For  $S = 1$ , the initial splitting  $\delta_{\pm 1}$  depends exclusively on the rhombic zero-field splitting parameter  $E$  and is given by  $\delta_{\pm 1} = 2E$ .

Moreover, the intensity of such integer-spin EPR transitions depends on  $\delta_{\pm 1}$  and is proportional to  $(g_z \delta_{\pm 1})^2 / (\hbar\nu)^2$ . Hence, finite rhombicity,  $E$ , is required for sufficient intensity, but the resulting energy gap  $\delta_{\pm 1}$  should not exceed the microwave quantum energy of  $\hbar\nu \approx 0.3$   $\text{cm}^{-1}$  at X-band frequencies.<sup>38–41</sup>

Numerical integration of the experimental parallel-mode derivative spectrum of the {Fe–NO}<sup>8</sup> species **3** revealed a maximum of the absorption around  $g^* \approx 9$ –10 and a gradual intensity drop toward higher fields (Figure 10, middle inset, black line). The intense low-field peak of this powder pattern stems from molecules oriented with their  $z$ -axes close to the field direction. These molecules exhibit a large Zeeman splitting (according to the easy  $z$ -axis of magnetization for “ $m_s = \pm 1$ ”) and, correspondingly, their resonances occur at low fields. According to the resonance expression, the Zeeman splitting for other orientations decreases quickly as the field deviates from the  $z$  direction, and higher field strengths are needed to cause resonance. The resulting large spread of resonance fields smears out intensities along the field axis and strongly attenuates the signal toward higher fields. A part of the powder spectrum may lay even beyond the range of the electromagnet. As a result of the steep absorption maximum, only the inflection points near the maximum give rise to the experimentally detected derivative spectrum.

Unexpectedly, the low-field edge of the numerically obtained absorption spectrum is significantly blurred and extends down to zero field, in contrast to the simulations vanishing below 50 mT (purple line in the inset). We suggest that the intensity smearing is due to heterogeneity of  $E/D$  values in the frozen solution ( $E/D$  strain). This causes scattering of  $\delta_{\pm 1}$  values for a fraction of the sample, including  $\delta_{\pm 1}$  values comparable to  $\hbar\nu$ , thus explaining the resonances at zero field already. For demonstration of the sensitivity of this intensity blurring on even very weak rhombic distortions, the inset of Figure 10 (middle) shows two simulations for slightly different  $E/D$  values (solid and dotted purple lines), which support the suggestion of a distribution of rhombicity values. The experimental derivative spectrum was simulated with fixed values of  $D$  and  $g_z$  taken from magnetometry, and merely  $E/D$  was optimized (purple line). The results infer that  $E/D$  is very close to zero and may vary up to 0.0046 or 0.0056, probably caused by structural heterogeneity in the frozen solution. In summary, the results corroborate the axial symmetry of **3**.

The zero-field <sup>57</sup>Fe Mössbauer spectrum of the {Fe–NO}<sup>8</sup> complex **3** shows a significantly larger quadrupole splitting than that of **2** ( $\Delta E_Q = +1.82$   $\text{mm s}^{-1}$  vs  $-0.51$   $\text{mm s}^{-1}$ , Table 2, Figure 11, middle panel). The positive sign of the quadrupole interaction was deduced from the 7 T applied field Mössbauer spectrum at 120 K (fast relaxation). All spectra, recorded in the temperature range of 1.7–12 K and fields of 4–7 T (B<sub>L</sub>γ), demonstrate only moderate magnetic splitting (Figure 11, middle panel, and Figure S20). This contrasts with the strong magnetization found in the SQUID and EPR measurements and implies that only a small component of the  $A$  matrix points along the easy axis of magnetization in the ground state of **3**. As the spin expectation

value  $\langle S \rangle$  for the low lying “ $m_s = \pm 1$ ” levels is primarily aligned in  $z$  direction,  $A_{zz}$  is small, and the internal field is essentially given by  $B_{\text{int}} \approx -A_{zz}\langle S_z \rangle / g_N \beta_N$ .

Remarkably,  $A_{zz}$  is positive as deduced from the increase of the magnetic splitting that is observed for the broad high-energy features with increasing applied fields from 4 to 7 T (Figure S20). This is unusual, as it means that very strong, anisotropic dipole or orbital contributions to the  $A$  matrix counteract the usually dominating negative and isotropic Fermi-contact contribution, and even invert the usually negative sign of all  $A$  components; details will be discussed below. Global simulations of the multifield spectra with  $D$ ,  $E/D$ , and the  $g$  matrix taken from EPR and SQUID analyses were also found to be sensitive for  $A_{xx/yy}$ , though with lower accuracy than for  $A_{zz}$ . The simulations yielded  $A/g_N\beta_N = (-16.5, -16.5, +9.5)$  T.

In summary, the pronounced asymmetry of the magnetic Mössbauer spectra of **3** can be assigned to competing magnetic Zeeman and electric quadrupole interaction with well-aligned, all-axial  $D$ , EFG, and  $A$  matrices, as expected for molecules with an idealized  $C_3$  symmetry. The quality of the fits is reasonable, considering a certain degree of irregularities in the powder distribution for the eicosane ( $C_{20}H_{42}$ ) embedded microcrystals. Most important, the field-dependence is well reproduced (SI).

**{Fe–NO}<sup>9</sup>**. Magnetization measurements of solid **4** revealed a temperature-independent effective magnetic moment  $\mu_{\text{eff}} = 1.88 \mu_B$  at room temperature, and weak field saturation below 20 K, as expected (Figure 9, bottom, brown trace). Accordingly, the total spin state of complex **4** was unambiguously assigned to  $S = 1/2$  ( $\mu_{\text{eff, s.o.}} = 1.73 \mu_B$ ) with an average  $g$  value of 2.19(10). Since a doublet ground state does not exhibit zero-field splitting, multifield measurements were not performed. In accordance with the SQUID data, the X-band EPR measurement of **4** (Figure 10, bottom) yielded an axial spectrum centered at  $g \approx 2$  with remarkably weak  $g$  anisotropy. Resolved hyperfine splitting at  $g_{\parallel}$  was assigned to superhyperfine coupling to the  $^{14}\text{N}$  nucleus of the nitrosyl ligand (99.63%,  $I = 1$ ). The simulation yielded the parameters  $g_{\perp} = 2.057$ ,  $g_{\parallel} = 2.024$ , and  $A_{\parallel} = 32$  MHz (nonresolved  $A_{\perp}$  splitting  $\approx 1.6$  MHz or less; Gaussian line widths  $W_{\parallel} = 19$  mT,  $W_{\perp} = 8$  mT).

Upon reduction of **3** to **4**, the isomer shift substantially decreased from  $\delta = 0.37 \text{ mm s}^{-1}$  (**3**) to  $0.17 \text{ mm s}^{-1}$  (**4**). The quadrupole splitting of **4**,  $\Delta E_Q = +2.73 \text{ mm s}^{-1}$  with  $\eta = 0$ , obtained from the zero-field and 5 T spectra recorded at 80 K, is significantly larger than that of **3** ( $\Delta E_Q = +1.82 \text{ mm s}^{-1}$ ). The low-temperature applied-field Mössbauer spectra of **4** (Figure 11, bottom right, and Figure S21) show magnetically perturbed quadrupole doublets with a shape asymmetry typical for positive  $\Delta E_Q$  and  $\eta = 0$ . Apparently, the internal fields are only weak to moderately strong. This is not unusual for  $S = 1/2$ , but interestingly, the (magnetic) splitting of the apparent line doublet at  $\approx +1.8 \text{ mm s}^{-1}$  slightly increases with applied field (5–7 T), whereas the splitting of the low-energy line-triplet ( $\approx -1.5 \text{ mm s}^{-1}$ ) significantly decreases (Figure S21). Both effects can be explained by the inherently different sensitivity of the involved  $m_I$  sublevels of the  $I = 3/2$  excited  $^{57}\text{Fe}$  nuclear state for hyperfine fields in  $z$  or in  $x/y$  directions. Apparently, the internal fields in  $x/y$  and  $z$  directions have opposite signs (details can be rationalized by using the concept of the effective nuclear  $g$  value<sup>42</sup>). Concluding from the anisotropy of the internal field, {Fe–NO}<sup>9</sup> (**4**) clearly has a

positive  $A_{zz}$  component aligned along the (positive) main component  $V_{zz}$  of the EFG, whereas the  $A_{xx}$  and  $A_{yy}$  components are negative. A global simulation of all VT-VF Mössbauer data with parameters summarized in Table 2 corroborated this interpretation of the experimental data.

**Electronic Absorption Spectroscopy of {Fe–NO}<sup>7–9</sup>**. The {Fe–NO}<sup>7–9</sup> complexes (**2–4**) with trigonal symmetry all show four bands in the UV/vis/NIR electronic absorption spectra (Figure 12). The band with the highest energy appears at  $\lambda_{\text{max}} = 260 \text{ nm}$  for all complexes and exhibits extinction coefficients of  $8100\text{--}14300 \text{ M}^{-1} \text{ cm}^{-1}$ . These values are characteristic for aryl  $\pi \rightarrow \pi^*$  transitions of the mesityl aryl rings.<sup>43</sup> The absorption bands at  $\lambda_{\text{max}} = 388 \text{ nm}$  (**2**) and  $348 \text{ nm}$  (**3**, **4**), with extinction coefficients  $\epsilon = 4.700 \text{ M}^{-1} \text{ cm}^{-1}$  (**2**, **3**) and  $3500 \text{ M}^{-1} \text{ cm}^{-1}$  (**4**), are typical and well-documented for Fe  $\rightarrow$  NHC charge-transfer bands.<sup>5,23</sup> The bands in the visible to near IR region ( $\lambda_{\text{max}} = 450$  to  $700 \text{ nm}$ ) are likely d–d transitions, given the relatively low extinction coefficients  $\epsilon = 350\text{--}550 \text{ M}^{-1} \text{ cm}^{-1}$ , respectively. With each reduction step to the neutral {Fe–NO}<sup>9</sup> complex (**4**), the Fe  $\rightarrow$  NHC as well as the d–d transitions show hypsochromic shifts upon reduction, whereas the  $\pi \rightarrow \pi^*$  transitions remain unchanged.

**DFT Calculations of {Fe–NO}<sup>7–9</sup> and Correlation of Their Electronic Structures with the Spectroscopic Properties.** Detailed theoretical calculations were carried out to shed more light on the electronic structures of complexes **2–4**. In order to account for antiferromagnetic coupling within the Fe–NO entity of **2–4**, DFT calculations were performed with the so-called “broken symmetry formalism”, denoted as BS( $m,n$ ) ( $m$  = unpaired electrons located at the iron center,  $n$  = electrons in the  $\pi^*$  orbitals of the NO ligand). Exploratory calculations—applying this formalism with different density functionals (B3LYP, BP86, and TPSSH) and varying initial guesses—consistently converged to one solution for each complex, viz., BS(5,2) for **2**, BS(4,2) for **3**, and BS(3,2) for **4** (for details, see Table S4). Comparing the computed key structural parameters of the {Fe–NO} <sup>$n$</sup>  complexes to the experimentally determined values of the molecular structure analyses showed that the most accurate results were obtained for the B3LYP functional. Generally, the error of the strong Fe–N(O) and N–O bonds is less than 0.01

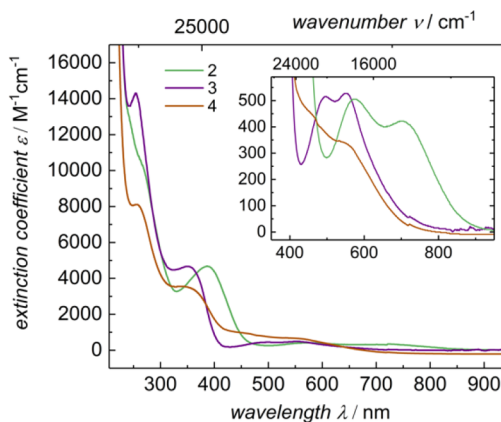


**Figure 12.** Electronic absorption spectra of the reduced Fe–NO complexes **2** (green trace), **3** (purple trace), and **4** (brown trace), measured at rt in acetonitrile (**2** and **3**) or THF (**4**). Inset shows the zoom in for transitions with lower extinction coefficients in the visible-light region.

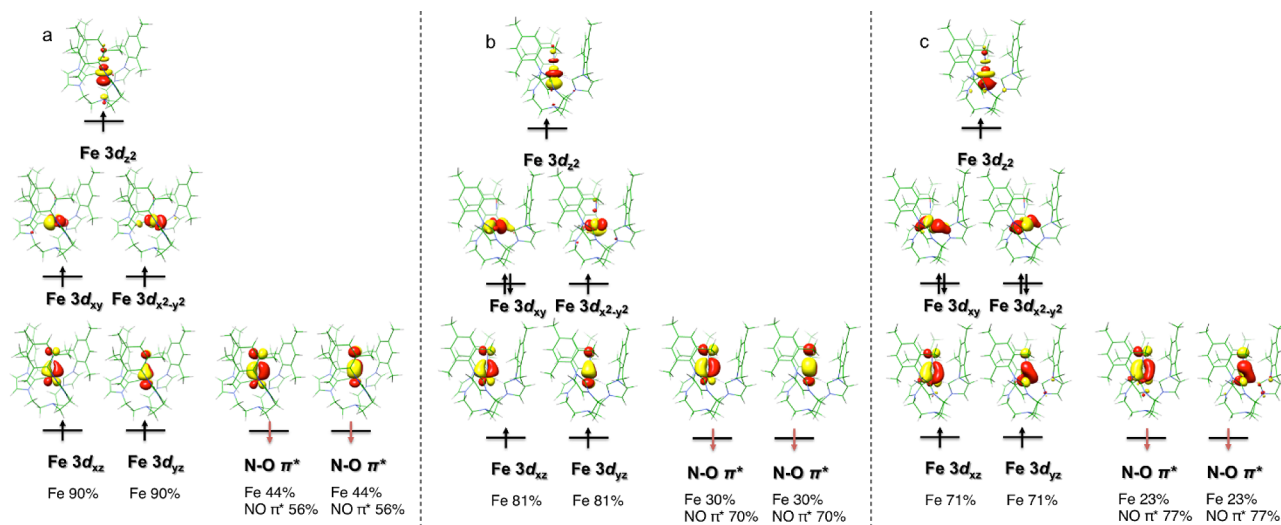


**Figure 13.** Calculated molecular orbital diagrams of complexes **2** (a), **3** (b), and **4** (c).

Å. The largest deviation (0.3 Å) was found for the weakest metal–ligand interaction, namely, the Fe–N<sub>anchor</sub> distance of **2** (Table S5).

The calculation of the spectroscopic parameters is of particular interest, as the comparison of the computational results with the experimental data provides an independent assessment of the proposed electronic structures for the {Fe–NO}<sup>n</sup> series presented here. The spectroscopic parameters of **2–4**, obtained from computed geometries, match the experimental data well. However, an even better agreement between theory and experiment was achieved with calculations based on the molecular geometries, determined by XRD analyses (H atom positions were optimized). This demonstrates that spectroscopic parameters are by far more sensitive to subtle geometry changes than the total energy itself. Therefore, the focus was placed on the computational results based on the experimentally determined geometries (summary of all theoretical results, see SI). The computed isomer shifts and quadrupole splittings are—within computational uncertainty—in excellent agreement with the experimental values (SI). Similarly, the calculated N–O stretching frequencies of 1835 cm<sup>-1</sup> (**2**), 1735 cm<sup>-1</sup> (**3**), and 1632 cm<sup>-1</sup> (**4**) are in satisfactory agreement with the experimental values.

**Physical Oxidation States and <sup>57</sup>Fe Mössbauer Spectroscopic Parameters.** Figure 13 depicts the schematic MO diagrams for the trigonal, axially symmetric complexes **2–4**, all featuring 2 + 2 + 1 ligand field splittings for the iron-centered d orbitals with e and a symmetry, e(3d<sub>xz/yz</sub>)–e(3d<sub>xy,x<sup>2</sup>-y<sup>2</sup>)–a(3d<sub>z<sup>2</sup></sub>) (also see Figures S35 and S36). Specifically, the Fe 3d<sub>xz/yz</sub> and 3d<sub>z<sup>2</sup></sub> orbitals interact with the π\* orbitals and the p<sub>z</sub> lone pair of the NO ligand, respectively. At the same time, the Fe 3d<sub>xy/x<sup>2</sup>-y<sup>2</sup></sub> orbitals accept electron density of the carbene σ lone pairs, but also donate electron density into the NHC unoccupied π\* orbitals. Note, NHC ligands are π accepting ligands.<sup>44</sup> This is possible because the NHC ring planes are largely perpendicular to the complex's equatorial plane. For the {Fe–NO}<sup>7</sup> species **2**, one can identify five singly occupied and clearly iron-based 3d orbitals in the spin-up manifold, whereas in the spin-down set two singly occupied MOs have nearly even contributions from the Fe 3d<sub>xz/yz</sub> and the NO π\* fragment orbitals. This indicates that the Fe–NO interaction is rather covalent, rendering an</sub>

unambiguous assignment of a physical oxidation state to the metal ion rather difficult. Under such circumstances, the most common description of **2** would be a resonance hybrid with a series of limiting electronic structures ranging from Fe(III) to Fe(I). However, given the relative weights of the Fe and NO character in the two highly mixed spin-down orbitals of **2**, one can conclude that the compound's electronic structure with a spin quartet ground state, S = 3/2, is predominantly composed of a high-spin Fe(III) center (S<sub>Fe</sub> = 5/2), antiferromagnetically coupled to a triplet <sup>3</sup>NO<sup>-</sup> ligand (S<sub>NO</sub> = 1).

Upon reduction of **2**, the iron 3d<sub>xy</sub> and 3d<sub>x<sup>2</sup>-y<sup>2</sup></sub> orbitals function as the electron-accepting orbitals, as can be inferred from the comparison of the MO diagrams for **2–4**. Hence, both reduction steps are metal-centered, and the nitroxyl ligand remains largely unchanged. As a consequence, the {Fe–NO}<sup>8</sup> complex **3** is best described as a high-spin Fe(II) center (S<sub>Fe</sub> = 2) that is antiferromagnetically coupled to a triplet NO<sup>-</sup> ligand (S<sub>NO</sub> = 1), yielding the total triplet ground state, S = 1. In fact, for ideal C<sub>3</sub> symmetry, **3** would feature an orbitally degenerate ground state because of the three electrons residing in degenerate 3d<sub>xy</sub> and 3d<sub>x<sup>2</sup>-y<sup>2</sup></sub> orbitals. However, Jahn–Teller distortion lifts this double degeneracy. Due to the crystallographically imposed 3-fold axes in crystals of **3**, structural distortions cannot be observed in the molecular structure. Finally, the {Fe–NO}<sup>9</sup> complex **4** possesses a high-spin Fe(I) center (S<sub>Fe</sub> = 3/2) interacting with a triplet <sup>3</sup>NO<sup>-</sup> ligand (S<sub>NO</sub> = 1) in antiferromagnetic fashion; thereby, affording an overall doublet ground state S = 1/2. The assignment of physical oxidation states to the iron centers in compounds **3** and **4** is more obvious than for **2**, because all key MOs have dominant character (≥70%) stemming either from the iron d shell or from the NO π\* orbitals.

Complexes **2–4** all contain a triplet <sup>3</sup>NO<sup>-</sup> ligand that is antiferromagnetically coupled to the majority spin at the Fe center. Thus, the NO<sup>-</sup> functions as a π acceptor in the spin-up manifold, whereas the nitroxyl ligand acts as a π donor in the spin-down set. As shown in Figure 13, in the spin-up manifold the degree of the π backdonation from the Fe center to NO is gradually increasing from **2** to **4**, as suggested by the attenuated Fe 3d character in the MOs labeled as Fe 3d<sub>xz,yz</sub>. At the same time, in the spin-down set, the π donation of NO declines as evidenced by the enhanced NO π\* weight in the MOs denoted

as N–O  $\pi^*$ ; hence, the  $\pi$  backdonation from the Fe center to NO reinforces in the spin-down manifold. Taken together, in both spin-up and spin-down sets, the  $\pi$  backbonding from Fe into the NO  $\pi^*$  orbitals strengthens upon reduction. This explains the successive shortening of the Fe–N(O) bonds as well as the N–O bond lengthening observed within the series 2–4. Qualitatively, the same findings were made for the reduction of  $\{\text{FeNO}\}^7$  to  $\{\text{FeNO}\}^8$  of the  $[(\text{TMG}_3\text{tren})\text{Fe}(\text{NO})]^{m+}$  ( $m = 2, 1$ ) series.<sup>28</sup> Analogously, a weakening of the N–O bond causes the observed red-shift of the NO stretching band. This is also in agreement with the assignment of metal-centered reductions and the comparatively small shifts of the NO stretching band through the complex series ( $\sim 125 \text{ cm}^{-1}$  on average, vide infra). In parallel to the intensified Fe–N<sub>NO</sub> interaction, the strength of the Fe–C<sub>NHC</sub> bond also increases via increasing  $\pi$  backbonding after each consecutive reduction, due to additional electrons occupying the iron  $3d_{xy}$  and  $3d_{x^2-y^2}$  based MOs. Hence, backbonding culminates at 4, as evidenced by the considerable electron density allocated to the NHC contributions to these two orbitals,<sup>44</sup> and explains the increasing contraction of the Fe–C<sub>NHC</sub> bonds within the series.

**Isomer shifts** are often used as spectroscopic markers to monitor changes in the physical iron oxidation state. Iron-based reductions of complexes with strong  $\sigma$  and  $\pi$  donors typically lead to more positive isomer shifts. However, this simple rule cannot be applied to systems featuring pronounced metal–ligand  $\pi$  backbonding, because—in addition to the occupation of the iron valence orbitals—the average iron–ligand bond length is a crucial factor in determining the value of the isomer shift. A detailed analysis recently rationalized that shorter iron–ligand bond distances generally cause lower isomer shifts.<sup>45</sup> Accordingly, the increased  $\pi$  backbonding of 3 compared to less reduced 2, phenomenologically evident from shorter Fe–N bond distances, counteracts the effect of the higher  $d^n$  occupation number. As a result, the difference in isomer shift between 2 and 3 is only marginal, merely  $0.06 \text{ mm s}^{-1}$ . This marginal difference is considerably smaller than the  $\sim 0.5 \text{ mm s}^{-1}$  commonly observed for changes of the isomer shift going from Fe(III) to Fe(II) high-spin sites. Moreover, the striking decrease of the isomer shift upon reduction of 3 to 4 likely arises from the substantial shrinking of the entire first coordination sphere. This seemingly counterintuitive behavior of the isomer shift variation has been observed before, and was thoroughly analyzed for the redox series  $[(\text{Si}^{\text{P}}\text{Pr}_3)\text{Fe}(\text{N}_2)]^{+/0/-}$  (with  $\text{Si}^{\text{P}}\text{Pr}_3 = [\text{Si}(o\text{-C}_6\text{H}_4\text{P}^{\text{P}}\text{Pr}_2)_3]^-$ ).<sup>46</sup>

**Quadrupole splitting** reflects the asymmetry of the electron density around the iron nucleus. Since a half-filled d-shell gives rise to a spherical distribution of valence electrons, the  $d^5$  high-spin Fe(III) ion assigned to complex 2 expectedly has the smallest quadrupole splitting of the series ( $\Delta E_Q = -0.51 \text{ mm s}^{-1}$ ). Upon reduction of 2, the additional electrons in the iron  $3d_{xy}$  and  $3d_{x^2-y^2}$  orbitals introduce asymmetry of the electron density, resulting in an increase in quadrupole splitting ( $\Delta E_Q = +1.82 \text{ mm s}^{-1}$  (3) and  $+2.73 \text{ mm s}^{-1}$  (4)). Note, the changes are significantly smaller than the value of  $4.5 \text{ mm s}^{-1}$  predicted for the addition of one “entire” d-electron to the  $3d_{xy}$  or  $3d_{x^2-y^2}$  orbitals in a basic crystal field model. The smaller  $\Delta E_Q$  differences can be attributed to considerable covalency of the metal–ligand interaction in complexes 2–4, as discussed above.

**Hyperfine interaction** contains three contributions of different physical origins to the coupling matrix  $A$ ; namely, the isotropic Fermi-contact term ( $A^{\text{FC}}$ ), the traceless spin-

dipolar term ( $A^{\text{SD}}$ ), and the orbital term ( $A^{\text{ORB}}$ ). While  $A^{\text{FC}}$  and  $A^{\text{ORB}}$  are proportional to the spin population of the iron center and the  $g$  shift, respectively,  $A^{\text{SD}}$  is a measure of the spin density deviation from spherical symmetry. The analysis of the EPR spectra of 4 revealed essentially isotropic  $g$  values close to 2 suggesting a quenched orbital angular momentum; hence, the orbital term can be safely neglected. This allows us to correlate any  $A$  anisotropy of the  $^{57}\text{Fe}$  hyperfine interaction reasonably well to dipole contributions ( $A^{\text{SD}}$ ), arising from asymmetry of the spin density distribution in the singly occupied valence orbitals.

The isotropic  $S = 1/2$  spectrum exhibits an internal field at the  $^{57}\text{Fe}$  nucleus according to  $A/g_N\beta_N = (-31, -31, +5.3) \text{ T}$ . The  $A^{\text{SD}}$  term can be estimated from the experimental  $A$  matrix simply by subtracting one-third of the trace ( $\sum A_{ii}/3 = -18.9 \text{ T}$ ). The resulting  $A^{\text{SD}}$  matrix ( $-12.1, -12.1, +24.2 \text{ T}$ ) is in good agreement with the DFT computed values ( $-12.1, -13.6, +25.7 \text{ T}$ ). Moreover, the sign and the ratio of the three  $A^{\text{SD}}$  components, being approximately  $(-1):(-1):2$ , is consistent with the “elongated” spin density distribution of the proposed  $(3d_{xy/x^2-y^2})^4(3d_{xz/yz})^2(3d_z)^1$  configuration. Since the isotropic Fermi-contact contribution  $A^{\text{FC}}$  is always negative and dominates the experimental  $A$  matrix of mononuclear iron complexes,  $A_{zz}$  should be the smallest component, as confirmed experimentally for 4. Furthermore, the  $g_{\parallel}$  component of the EPR spectrum reveals resolved hyperfine coupling to the  $^{14}\text{N}$  nucleus of the nitrosyl ligand ( $A = 32 \text{ MHz}$ ). However, the isotropic  $A_{\text{iso}}(^{14}\text{N})$  value of  $\sim 12 \text{ MHz}$ —at most—is much lower than the values of 46 and 27.3 MHz reported for the mono and dinuclear complexes  $[(\text{tpp})\text{Fe}(\text{NO})]^{47}$  and  $[\{(\text{Me}_3\text{Si})_2\text{N}\}_2(\text{THF})\text{Y}\}_2(\mu\text{-NO})]$  with diamagnetic central metal ions and paramagnetic  $\text{NO}^\bullet$  and  $\text{NO}^{2-}$  ligands, respectively.<sup>48</sup> If the usual spin projection technique is applied to estimate the “on-site”  $A_{\text{iso}}(^{14}\text{N})$  value of 4, with  $\text{Fe}(\text{I})$ ,  $S_{\text{Fe}} = 3/2$ , and the  $\text{NO}^-$  ligand  $S_{\text{NO}} = 1$ ,  $A_{\text{iso,NO}}(^{14}\text{N})$  is estimated at 18 MHz ( $3/2$  times the experimental value with respect to the total spin  $S = 1/2$ ). Thus, the magnetic NO  $\pi^*$  orbitals appear to be “diluted” due to  $\pi$  backbonding and covalence, resulting in a reduced, experimental observed N superhyperfine coupling.

In analogy to 4, the  $A^{\text{SD}}$  matrix of 2 can also be estimated from the experimental  $A$  anisotropy without considering orbital contributions. The result,  $(+1.2, +1.2, -2.4 \text{ T})$ , is consistent with the DFT computed  $A^{\text{SD}}$  matrix of  $(+1.6, +1.5, -3.1 \text{ T})$ . The small anisotropy is readily compatible with the assignment of a high-spin Fe(III) ion in 2 with a half-filled d shell. In general, the spin-Hamiltonian parameters ( $g$ ,  $D$ , and  $E/D$ ) determined for 2 are comparable to those reported for  $[(\text{TMG}_3\text{tren})\text{Fe}(\text{NO})]^{2+}$ ,<sup>5</sup> both complexes featuring a similar coordination geometry. Interestingly, the anisotropy of the  $A$  matrix ( $-21.0, -20.4, -30.0 \text{ T}$ ) measured for  $[(\text{TMG}_3\text{tren})\text{Fe}(\text{NO})]^{2+}$  and the resulting dipole contribution  $A^{\text{SD}}$  are significantly larger than for 2. This difference likely is due to the fact that the NO and NHC ligands in 2 are both  $\sigma$  donors and  $\pi$  acceptors, whereas  $\text{TMG}_3\text{tren}$  is merely a  $\sigma$  donor. Thus, the anisotropic metal–ligand interaction in  $[(\text{TMG}_3\text{tren})\text{Fe}(\text{NO})]^{2+}$  causes a more anisotropic  $A^{\text{SD}}$  matrix.

Also, the isotropic  $A_{\text{iso}}$  value of 2 ( $-16.5 \text{ T}$ ) is considerably smaller than that of  $[(\text{TMG}_3\text{tren})\text{Fe}(\text{NO})]^{2+}$  ( $-23.8 \text{ T}$ ). The nearly isotropic, intrinsic  $g$  ( $\sim 2$ ) matrices of both  $\{\text{Fe–NO}\}^7$  complexes allow to rule out orbital contributions, and the distinctly smaller isotropic  $A_{\text{iso}}$  value of 2 must originate from a reduced Fermi contact contribution,  $A^{\text{FC}}$ , due to a higher

degree of Fe–NO covalency. This is in accordance with a lower spin population at the iron center, mainly caused by  $\pi$  backbonding of Fe  $3d_{xz/yz}$  fragment orbitals with the two NO  $\pi^*$  MOs of **2** (Figure 13a).

**Unquenched Orbital Moment for 3.** Typically, the  $g$  anisotropy of transition metal complexes is largely dictated by spin–orbit coupling (SOC). Thus, the degree of unquenched orbital moment determines the so-called “ $g$  shift”, the difference between the experimentally determined  $g$  value and the spin-only value,  $g_{s.o.} = 2$ . SOC can be treated in terms of single-electron excitations. The excitation of an electron from a doubly to a singly occupied MO results in a positive shift of the  $g$  component, defined by the rules of the angular momentum operator connecting the states. Similarly, an excitation from a singly occupied to a virtual (empty) MO gives rise to a negative  $g$  shift. The magnitude of the  $g$  shift is inversely proportional to the associated excitation energy, i.e., the energy difference between the respective MOs.

The iron center of **3** possesses an electron configuration  $(3d_{xy/x^2-y^2})^3 (3d_{xz/yz})^2 (3d_z^2)^1$ , with one hole in the nearly degenerate Fe  $3d_{xy}$  and  $3d_{x^2-y^2}$ -based MOs of the effective  ${}^3E$  ground state. The energy of the  $d_{xy} \rightarrow d_{x^2-y^2}$  excitation is  $371 \text{ cm}^{-1}$ , as obtained from TD-DFT. The corresponding transition induces large SOC and results in a positive  $g$  shift along the  $z$ -axis. This mechanism explains the observed large  $g_z$  value of 2.78, as well as the substantially negative  $D$  value of **3**. Quantitatively, an effective  $g$  factor of  $2g_z = 8$  is predicted for the *quasi*  $\Delta m = 2$  transition between the “ $m_s = \pm 1$ ” levels of a triplet state in an idealized case with three electrons occupying two, exactly degenerate, pure metal  $3d_{xy}$  and  $3d_{x^2-y^2}$  orbitals. The observation that the experimentally determined *effective*  $g$  factor of  $2g_z = 5.56$  (**3**) is much lower than 8 can be readily attributed to the considerable metal–ligand covalency and the geometric distortion that lifts the double degeneracy of the  ${}^3E$  ground state.

The analysis of the pronounced  $A$  anisotropy of **3** as well as the spin-dipole part  $A^{\text{SD}}$  require consideration of the orbital contribution  $A^{\text{ORB}}$ . According to the measured  $g$  values of **3** ( $g_x = g_y = 2.02$  and  $g_z = 2.78$ ), the  $z$  component of  $A^{\text{ORB}}$  is expected to be substantially larger than zero, and the  $x/y$  components should be close to zero. The Fe–NO and Fe– $C_{\text{NHC}}$  interactions are largely isotropic also observed for **2**. Under the assumption that the covalency of all metal–ligand interactions is uniformly increasing within the redox series  $\{\text{Fe–NO}\}^{7,8,9}$ , one can estimate the  $A^{\text{SD}}$  contribution of **3** to be the average of the experimentally determined  $A^{\text{SD}}$  matrices of **2** and **4**. This is justified because complexes **2**, **3**, and **4** have nearly identical electron configurations with the only variable being the different number of electrons residing in the Fe  $3d_{xy}$  and  $3d_{x^2-y^2}$  centered MOs. The resulting  $A^{\text{SD}}$  matrix ( $-5.9, -5.9, +11.8 \text{ T}$ ) agrees with the DFT results,  $A^{\text{SD}} = (-4.8, -5.4, +10.1 \text{ T})$ . However, the computed  $A$  anisotropy ( $\sim 23 \text{ T}$ ) is significantly lower than the experimentally determined value ( $\sim 52 \text{ T}$ ) because the magnitude of  $A^{\text{ORB}}$  is substantially underestimated by DFT that cannot accurately treat the magnetic effects arising from the orbitally nearly degenerate ground state of **3**. Despite this deficiency, one can conclude that both  $A^{\text{ORB}}$  and  $A^{\text{SD}}$  contributions add up, and mutually strengthen each other, resulting in the largely anisotropic  $A$  matrix of **3**.

**Reduction to the  $\{\text{Fe–NO}\}^{10}$  Intermediate and Formation of a Nitrosoalkane Complex by N-Migratory Insertion of the Coordinated NO into the Fe–Carbene**

**Bond.** The reduction of the  $\{\text{Fe–NO}\}^9$  complex **4** was accomplished by addition of a so-called “electride” solution, commonly termed as a solution of dissolved electrons prepared from elemental cesium and crypt-222 in THF. Reaction of this solution with **4**, in frozen THF at  $-110 \text{ }^\circ\text{C}$ , results in formation of the highly reduced  $\{\text{Fe–NO}\}^{10}$  fleeting intermediate and, subsequently, in the isolation of the nitrosoalkane complex  $[\text{Cs}(\text{crypt-222})][(\text{TIMEN}^{\text{Mes}})\text{Fe}(\text{NO})]$  (**5**). This reaction likely proceeds via migratory N insertion of the coordinated nitric oxide into one of the iron–carbene bonds of the chelating tris-NHC ligand, and is reminiscent to what Weiner and Bergman described for the reduction of  $[(\text{Cp})\text{Co}(\text{NO})]$  with Na/Hg, followed by addition of an alkyl halide and phosphine.<sup>49</sup>

**NMR Spectroscopy of  $[\text{Cs}(\text{crypt-222})][(\text{TIMEN}^{\text{Mes}})\text{Fe}(\text{NO})]$  (**5**).** The  ${}^1\text{H}$  NMR spectrum of the crude  $[\text{Cs}(\text{crypt-222})][(\text{TIMEN}^{\text{Mes}})\text{Fe}(\text{NO})]$  (**5**) (Figure 14 and Figure S4) was recorded immediately after reduction of the  $\{\text{Fe–NO}\}^9$  in THF- $d_8$  at  $23 \text{ }^\circ\text{C}$ . The nonmagnetic ground state with  $S = 0$  exhibits, as expected, exclusively signals in the diamagnetic shift range. Contrary to the  $C_3$ -symmetric complexes  $\{\text{Fe–NO}\}^{7-9}$  (**2–4**) but similar to  $\{\text{Fe–NO}\}^6$  (**1**) (vide supra), the observed multiple sets of signals for each type of protons suggest a  $C_s$ -symmetric molecular structure of **5** in solution. Due to its thermal instability, all further NMR investigations (400 MHz;  ${}^1\text{H}$ ,  ${}^1\text{H}$ – ${}^1\text{H}$  COSY,  ${}^{13}\text{C}$ , and  ${}^1\text{H}$ – ${}^{13}\text{C}$  HMQC as well as HMBC spectra) were conducted in THF- $d_8$  at  $-20 \text{ }^\circ\text{C}$ , which allowed for the unequivocal assignment of all proton resonances. As for  $\{\text{Fe–NO}\}^6$  (**1**), the nine methyl groups of the mesityl substituents in **5** appear as sharp singlets in the diamagnetic range between 2.27 and 1.26 ppm, established by integration and the correlation experiments (Figure 14, resonances a/a'). Furthermore, the 12 proton resonances of the ethylene bridges result in nine signals between 5.20 and 2.67 ppm (Figure 14, b/b'). Two of these signals are caused by five accidentally isochronous protons and four protons appear as well-resolved doublets of doublets, indicating a rather similar conformation in the N-anchored TIMEN<sup>Mes</sup> ligand system compared to  $\{\text{Fe–NO}\}^6$  (**1**) (vide supra). This spectral range (5.20 bis 2.52) is further dominated by three broad singlets of the three magnetically inequivalent methylene groups of the  $[\text{Cs}(\text{crypt-222})]^+$  cation (3.57, 3.48, and 2.53 ppm; 12 H each). In the aromatic region, six singlets (6.85 to

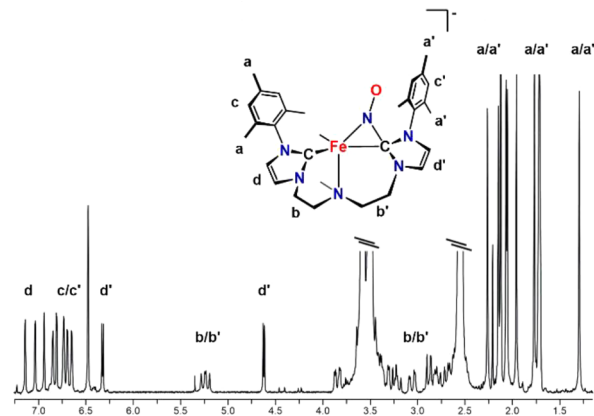


**Figure 14.**  ${}^1\text{H}$  NMR spectrum of **5**, measured at 270 MHz in THF- $d_8$  at room temperature. One arm of the tripodal NHC-ligand in the molecule depiction is omitted for clarity.

6.47 ppm; Figure 14, c/c') and four doublets (7.21 to 6.85 ppm, Figure 14, d) are assigned to the protons of the mesityl and imidazole-2-ylidene group, respectively. The two remaining imidazole-2-ylidene protons are strongly high-field shifted, resulting in resonances at 6.30 and 4.64 ppm (Figure 14, d'), respectively. These smaller chemical shifts can be explained by increasing electron density on the  $^1\text{H}$  protons, resulting from an electronic structure change of the chelating ligand framework (e.g., caused by a  $\mu\text{-NO}$  bridging Fe–C carbene bond, *vide infra*).

A  $C_s$ -symmetric molecular structure of **5** is also observed in the  $^{13}\text{C}$  NMR spectrum (101 MHz,  $\text{THF-}d_8$ ,  $-20\text{ }^\circ\text{C}$ ), where all carbon atoms of the  $\text{TIMEN}^{\text{Mes}}$  ligand give rise to one carbon resonance with the only exception of the  $\mu\text{-NO}$ -bridged Fe–C atom, which could not be detected. Most notably, the signals of the two other NHC Fe–C atoms are highly downfield shifted (216.29 and 208.26 ppm) compared to the  $\{\text{Fe-NO}\}^6$  (**1**; *vide supra*). These signals were unequivocally identified based on the corresponding cross peaks between these carbon atoms and the two corresponding imidazole-2-ylidene protons in the  $^1\text{H-}^{13}\text{C}$  HMBC spectrum.

**IR Vibrational Spectroscopy of  $\{\text{Fe-NO}\}^{6-9}$  and **5**.** The trend of NO stretching frequency observed for the series of nitrosyl complexes directly correlates with the steady increase of the N–O bond distance and associated decrease of bond strength. The relatively small shift of the N–O stretching band per additional electron is commonly observed for metal-centered reductions of Fe–NO complexes. It is caused by an indirect increase of electron density in the NO  $\pi^*$  orbitals through  $\pi$  backbonding from the iron center.<sup>5,6,30</sup> This  $\pi$ -backbonding, in turn, causes shortening of the Fe–N bond, as determined by XRD analyses. The direct occupation of the  $\pi^*$  orbitals through ligand-based reduction would lead to a stronger than observed bathochromic NO band shift of about  $300\text{ cm}^{-1}$ .<sup>15,50</sup> Noteworthy, all observed NO stretching frequencies of **2**, **3**, and **4** are  $40\text{--}100\text{ cm}^{-1}$  higher than most reported Fe–NO complexes with the corresponding number of valence electrons in its unit.<sup>5,30,51,52</sup> The successful reduction of the  $\{\text{Fe-NO}\}^9$  (**4**) to the nitrosoalkane complex **5** also was confirmed by IR vibrational spectroscopy. The intense NO stretching band  $\tilde{\nu}_{\text{NO}} = 1550\text{ cm}^{-1}$  of **4** is shifted to  $1358\text{ cm}^{-1}$  upon reduction to **5**. This bathochromic shift is larger than observed for all other previous complexes after reduction (Figure 15) and is indicative of the strongest weakening of the N–O bond. However, the observed band at

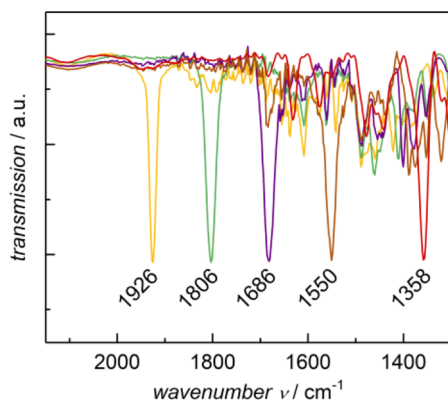


**Figure 15.** NO stretching bands in the IR spectra of **1** (yellow), **2** (green), **3** (purple), **4** (brown), and **5** (red); KBr disks measured at rt.

$1358\text{ cm}^{-1}$  compares well with a vibration band centered at  $1310\text{ cm}^{-1}$  reported for the NO insertion product  $[(\text{Cp})\text{Co}(\text{N}(\text{O})\text{CH}_3)(\text{PPh}_3)]$  by Weiner and Bergman.<sup>49</sup> Apart from the bathochromic NO band shift, the overall IR vibrational spectrum is similar for all the  $\{\text{Fe-NO}\}^{6-9}$  complexes.

**VT-VF  $^{57}\text{Fe}$  Mössbauer Spectroscopy of **5**.** The VT-VF  $^{57}\text{Fe}$  Mössbauer spectra of solid samples of **5** reveal diamagnetism with a total spin  $S = 0$  and the absence of internal field at the  $^{57}\text{Fe}$  nucleus (Figure 16). The Mössbauer parameters determined by simulation were  $\delta = 0.05(1)\text{ mm s}^{-1}$ ,  $\Delta E_{\text{Q}} = 1.35(1)\text{ mm s}^{-1}$ ,  $\Gamma_{\text{fwhm}} = 0.31(1)\text{ mm s}^{-1}$ , and  $\eta = 0.82$ . The isomer shift follows the decreasing trend observed for the reduction of **3** to **4** and **4** to **5**.

At first sight, this observation suggests another metal-centered reduction step, *viz.*  $\{\text{Fe-NO}\}^9$  to  $\{\text{Fe-NO}\}^{10}$ . However, the large asymmetry parameter  $\eta$  of **5** is unusual, implying a less straightforward interpretation. While the series of  $\{\text{Fe-NO}\}^{7-9}$  species **2–4** has  $\eta = 0$  values, thus, supporting axial  $C_3$  symmetry, **5** possesses an  $\eta$  of 0.82, more reminiscent to that of **1** (Table 3). This clearly indicates that reduced **5** is not  $C_3$ - but  $C_s$ -symmetric like **1**. Complex **5** is exceedingly air and temperature sensitive, and all attempts to obtain single crystals for structural analysis remained elusive.

**DFT Calculations of **5**.** DFT calculations gave further insight into the molecular and electronic structure of the highly reduced nitrosoalkane complex **5**. Different structural models of **5** were tested by employing the B3LYP density functional with closed-shell singlet and broken-symmetry calculations (for details, see the SI).

The only structural model that successfully reproduces the spectroscopic properties of **5**, within computational error (SI),

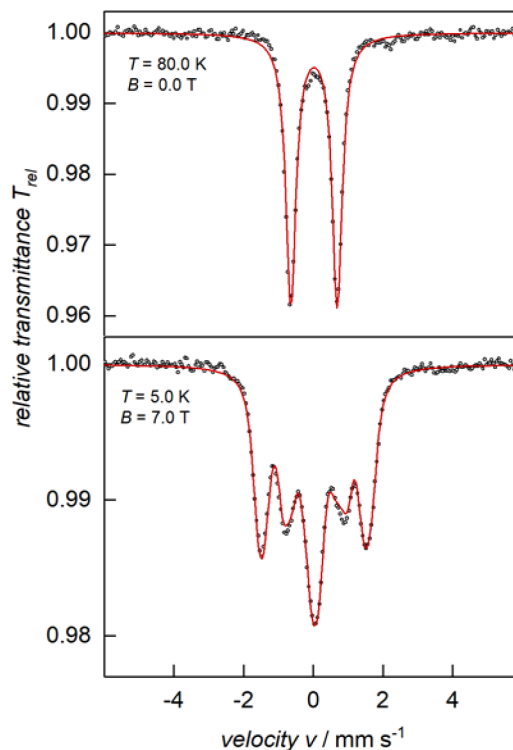


**Figure 16.** VT-VF  $^{57}\text{Fe}$  Mössbauer (B $\perp\gamma$ ) spectra of **5**, powder sample recorded at 80 and 5 K with fields of 0 (top) and 7.0 T (bottom). The red line represents the best fit obtained with  $S = 0$  and  $\delta = 0.05\text{ mm s}^{-1}$ ,  $\Delta E_{\text{Q}} = 1.35\text{ mm s}^{-1}$ ,  $\Gamma_{\text{fwhm}} = 0.31\text{ mm s}^{-1}$ ,  $\eta = 0.82$ .

**Table 3.**  $^{57}\text{Fe}$  Mössbauer Parameters of Diamagnetic **5** and  $\{\text{Fe-NO}\}^6$  Species **1** for Comparison; Isomer Shift,  $\delta$ , Quadrupole Splitting,  $\Delta E_{\text{Q}}$ , Line Width,  $\Gamma_{\text{fwhm}}$ , All in Units of  $\text{mm s}^{-1}$

	$\{\text{Fe-NO}\}^6$ <b>1</b>	$[\text{Fe-NO-NHC}]$ <b>5</b>
$S$	0	0
$\delta$	0.02	0.05
$\Delta E_{\text{Q}}$	+2.40	+1.35
$\Gamma_{\text{fwhm}}$	0.26	0.31
$\eta$	0.74	0.82

features an iron-bound  $(\text{NO-NHC})^{3-}$  metalacyclic moiety (Figure 17), with a uniquely short  $\text{N}_{\text{NO}}-\text{C}_{\text{NHC}}$  bond of 1.421 Å, and an elongated  $\text{Fe-NO}$  bond of 1.746 Å, which is much longer than the corresponding distance of **4**. The other  $\text{Fe-C}_{\text{NHC}}$  distances (1.968 Å) as well as the  $\text{N}_{\text{NO}}-\text{O}$  distance (1.288 Å) are nearly unchanged compared to **4**. Again, comparison of the metrics of **5** to Bergman's NO insertion product  $[(\text{Cp})\text{Co}(\text{N}(\text{O})\text{Et})(\text{PPh}_3)]$ , with  $d(\text{Co}-\text{N}_{\text{NO}}) = 1.780$  Å,  $d(\text{N}_{\text{NO}}-\text{O}) = 1.282$  Å, and  $d(\text{N}_{\text{NO}}-\text{C}_{\text{Et}}) = 1.484$  Å is excellent.

Electronically, calculated **5** has a closed-shell singlet ground state with the three  $t_{2g}$ -derived orbitals of the iron center fully occupied (Figure 18 and Figure S36). For the  $(\text{NO-NHC})^{3-}$  motif of the chelator, the computation reveals two MOs representing the N-O and N-C  $\sigma$  bonding orbitals, in addition to two O- and one N-based 2p lone pairs (LPs). Finally, a 2s N-based lone pair forms a dative bond with the Fe center. This orbital pattern endorses a low-spin Fe(II) center bound to the diamagnetic  $(\text{NO-NHC})^{3-}$  trianionic ligand, arising from nucleophilic attack of the  $\text{NO}^{3-}$  on the N-heterocyclic carbene ligand. During the formation of the N-C single bond, the originally  $\text{sp}^2$ -hybridized NHC carbon atom rehybridizes to  $\text{sp}^3$ , consistent with the carbon center's nonplanar geometry.

The small isomer shift of **5** is attributed to the formation of a closed-shell,  $d^6$ ,  $[\text{Fe}^{\text{II}}-(\text{NO-NHC})^{3-}]$  complex and not to the shortening of the  $\text{Fe-N}$  and  $\text{Fe-C}$  bonds as observed for **2-4**. The quadrupole splitting parameter is reduced to  $\Delta E_{\text{Q}} = +1.35$   $\text{mm s}^{-1}$  (from  $\Delta E_{\text{Q}} = +2.73$   $\text{mm s}^{-1}$  in **4**) due to the

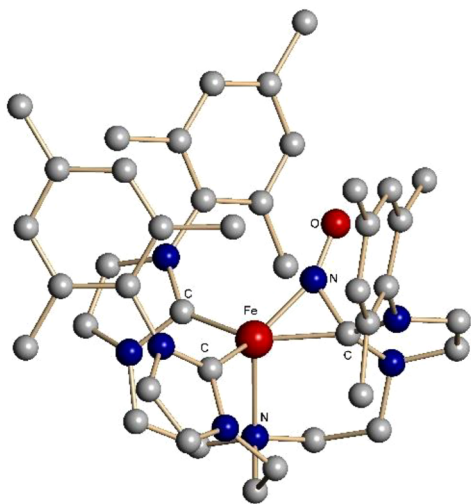


**Figure 17.** Calculated molecular structure of the anion of  $[\text{Cs}(\text{crypt-222})][(\text{TIMEN}^{\text{Mes}})\text{Fe}(\text{NO})]$  (**5**) with its metalacyclic  $[\text{Fe}-(\text{NO-NHC})^{3-}]$  core unit.

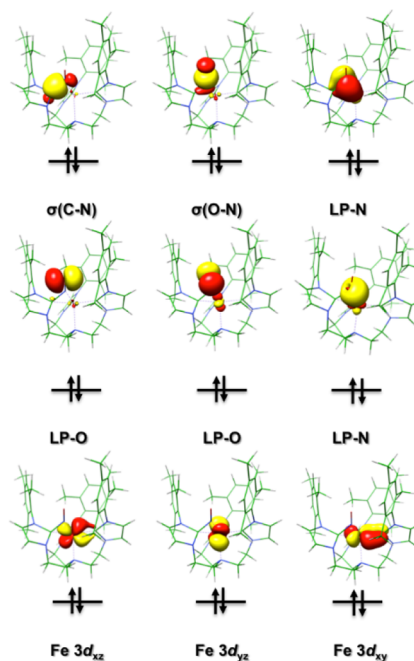
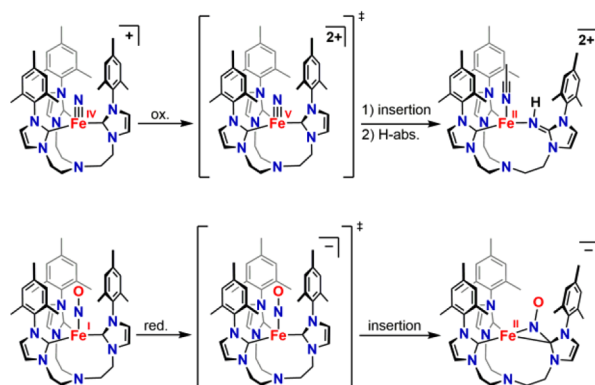


**Figure 18.** Calculated molecular orbital diagram of **5**.

predominantly even distribution of  $d$  electrons around the closed-shell iron center together with the electrons of the C-N and N-O  $\sigma$  bonds of the newly formed  $(\text{NO-NHC})^{3-}$  unit. Due to the overall loss of complex symmetry,  $\Delta E_{\text{Q}}$  of reduced **5** is still relatively large, while being smaller than that of  $\{\text{Fe-NO}\}^9$ . This is further supported and substantiated by the computed large asymmetry factor of  $\eta = 0.82$ .

The metalacyclic  $[\text{Fe}^{\text{II}}-(\text{NO-NHC})^{3-}]$  unit of **5**, as shown in Figure 17, is formed by incomplete NO insertion into an  $\text{Fe-C}_{\text{NHC}}$  bond. This reaction not only is parallel to Bergman's migratory NO insertion<sup>49</sup> but also is remarkably similar to the recently reported imido insertion in a Co(IV) species,<sup>53</sup> and the nitride ( $\text{N}^{3-}$ ) insertion (with subsequent H abstraction) observed for the high-valent nitrido complex (Scheme 2) supported by the polydentate tris-NHC ligands  $\text{TIMEN}^{\text{R}}$ .<sup>23,54</sup> Upon one-electron oxidation, the tetravalent nitrido complex  $[(\text{TIMEN}^{\text{Mes}})\text{Fe}(\text{N})]^+$  yields a bis-carbene mono-imine species by N-migratory insertion of the nitrido ligand into the  $\text{M-C}_{\text{NHC}}$  bond.<sup>23</sup>

### Scheme 2. Reaction Scheme for Complete Nitride and Incomplete Nitrosyl Insertion



Useful information on the formation of the  $(\text{NO-NHC})^{3-}$  motif, here of **5**, is given in a recent report on the formation of stable NHC adducts,  $\text{NHC-NO}$ , where  $\pi$  backbonding from NO to the empty carbene p orbital is invoked.<sup>55–57</sup> In the series of  $\{\text{Fe-NO}\}^{6-9}$  complexes, and further reduction to **5** via intermediate  $\{\text{Fe-NO}\}^{10}$ , electron density unexpectedly is predominantly added to the central Fe ion upon successive reduction. Due to enhanced  $\pi$  bonding from Fe to NO (evidence from  $^{57}\text{Fe}$  Mössbauer isomer shifts and quadrupole splittings, vide supra), the reduction concurrently builds up charge on the nitrosyl N atom (see decreasing Fe–N and increasing Fe–O bond distances). The electron-rich nitrosyl N in the intermediate  $\{\text{Fe-NO}\}^{10}$  inserts into the Fe–carbene bond, thereby acting similar to a nitride forming the N-migratory insertion of the complex derivative discussed above.

**Transformation of a High-Valent Metal Nitride to a Low-Valent Metal Nitrosyl Upon Oxygenation – Where Do the Electrons Go?** Inspired by the nitride analogy (vide supra), an alternative entry to the series of iron nitrosyl complexes was sought by starting from an appropriate iron nitride precursor and an oxygen atom transfer (OAT) reagent. Interestingly, the reaction of  $[(\text{TIMEN}^{\text{Mes}})\text{Fe}(\text{N})]^+$  with trimethylamine-*N*-oxide,  $\text{Me}_3\text{NO}$ , in acetonitrile at room temperature, merely leads to a slight color change. Following the reaction by UV/vis electronic absorption spectroscopy (Figure 19) corroborates the visual interpretation of the course and completeness of reaction. Isolation and characterization of the reaction product by single-crystal XRD analysis, IR vibrational,  $^{57}\text{Fe}$  Mössbauer, and combustion analysis (see the SI) confirms the formation of  $[(\text{TIMEN}^{\text{Mes}})\text{Fe}(\text{NO})]^+$  via oxygenation of the corresponding iron nitride. The product of the nitride oxygenation is identical to the  $\{\text{Fe-NO}\}^8$  species **3** described above.

Similar to what has been observed for the first ever reported nitride-to-nitrosyl oxidation to  $[(\text{tpy})\text{Os}(\text{N/O})(\text{Cl})_2]^+$  by Meyer et al., there is no evidence for the formation of intermediates and the heterolytic N–O bond breakage, O atom transfer, and  $\text{NMe}_3$  elimination appears to be synchronous.<sup>58,59</sup> It is interesting to note that the latter report is titled “Preparation of Osmium(II) Nitrosyls by Direct Oxidation of Osmium(VI) Nitrides”, with explicit stating of the “formal four-electron change at the metal.” In 1998, Mayer

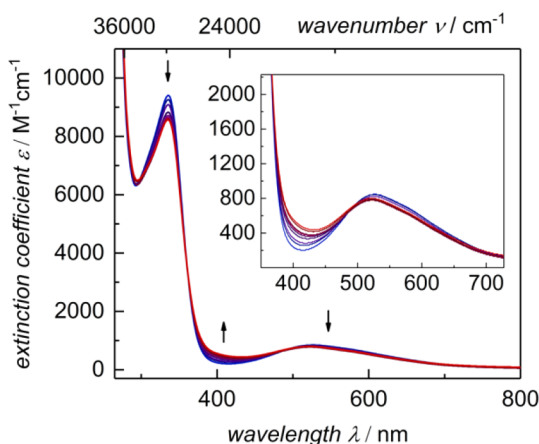


**Figure 19.** Electronic absorption spectra of the OAT reaction of  $[(\text{TIMEN}^{\text{Mes}})\text{Fe}(\text{N})]^+$  (blue trace) complex toward the  $\{\text{Fe-NO}\}^8$  (**3**, red trace) measured at rt in acetonitrile. Inset shows the zoom for transitions with lower extinction coefficients in the visible-light region.

and co-workers reported a similar reactivity, employing  $[(\text{Tp})\text{Os}(\text{N})(\text{Cl})_2]^+$  and  $\text{Me}_3\text{NO}$  to yield  $[(\text{Tp})\text{Os}(\text{NO})(\text{Cl})_2]^+$ , without mentioning of any formal oxidation state changes.<sup>22</sup>

These literature reports of nitride oxygenations are remarkable in that they exemplify rare cases of multielectron ligand transformations, viz. nitride-to-nitrosyl (and vice versa, for nitrosyl deoxygenation<sup>60</sup>). However, this reaction often is referred to as a transformation of a *high-valent* metal nitrido to a *low-valent* metal nitrosyl complex, hence implying—explicitly or intuitively—a four-electron metal-centered reduction reaction even though atomic [O] oxygen is being transferred.

The first report questioning these implications came from Bendix, Wieghardt, and co-workers in 1998.<sup>61</sup> Since one would expect a “dramatic structural change between two complexes of similar composition, where the formal oxidation states vary by four units,” the authors tackle the issue of the complexes’ formal oxidation state and how electronic and structural parameters change within the pair of complexes  $\text{M}^n\equiv\text{N}/\text{M}^{(n-4)}-\text{NO}$ . The authors note that in a number of those complex pairs the M–L metric parameters are nearly equidistant. More importantly, it is realized that the  $\tilde{\nu}(\text{CN})$  wavenumbers in  $[(\text{NC})_4\text{Re}(\text{N}(\text{O}))(\text{OH})_2]^{2-}$  are “very similar, indicating similar bonding (and electron densities at the central metal ions) in the nitrido and corresponding nitrosyl species.” Consequently, the authors propose a nomenclature for metal nitrido complexes in accordance to the Enemark–Feltham formalism for nitrosyl complexes, and suggest “the notation  $\{\text{M-N}\}^n$ , where  $n$  gives the number of d electrons in this diatomic moiety if the nitrido ligand is formally counted as a tri-negatively charged, two-electron donor.”<sup>61</sup> This approach is further supported by a more recent DFT/TD-DFT computational analysis and report by Hummel, Winkler, and Gray, who state that the electronic structures of metal nitride and nitrosyl complexes  $[(\text{L})\text{M}(\text{N}(\text{O}))]^z$ , with the same overall charge ( $z$ ) and in tetragonal symmetry, is strikingly similar.<sup>62</sup>

Upon close inspection of the here-presented pair of trigonal complexes  $[(\text{TIMEN}^{\text{Mes}})\text{Fe}(\text{N}(\text{O}))]^+$  (Figure 20), we support this approach but suggest counting the nitrido ( $\text{N}^{3-}$ ) ligand not only a 2-electron  $\sigma$  but a 4-electron  $\pi$  donor as well. Together with the four metal d electrons within the  $\text{Fe}\equiv\text{N}$  orbital framework of  $[(\text{TIMEN}^{\text{Mes}})\text{Fe}^{\text{IV}}(\text{N})]^+$ , this nitrido complex would have to be counted as  $\{\text{Fe-N}\}^8$ —or generally speaking  $\{\text{M-N}\}^{n+4}$ . To simplify the analysis of the electron

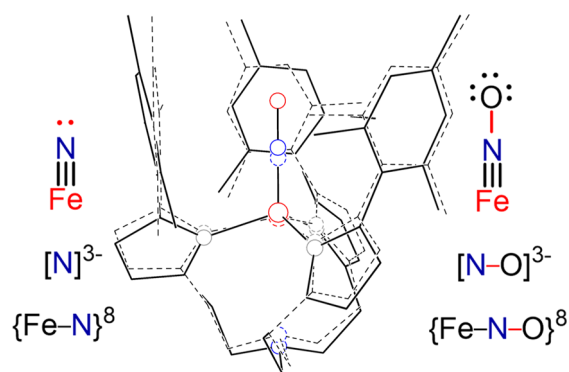


**Figure 20.** Structural overlay of cationic  $\{\text{Fe-NO}\}^8$  (**3**) (solid line) and  $[(\text{TIMEN}^{\text{Mes}})\text{Fe}^{\text{IV}}(\text{N})]^+$  (dashed line), with the proposed nomenclature for metal nitrides in accordance with the Enemark–Feltham formalism for nitrosyl complexes.

count, we assume that the metal  $d^n$  electron count does not change for a metal–nitrido/nitrosyl pair of complexes. In this picture, during the nitride oxygenation, a charge-neutral oxygen atom, [O], is transferred to the nitride and the formal oxidation state of the metal ion ( $M^{n+}$ ) remains unaffected. As a consequence, the resulting nitrosyl complex would be formulated as  $M^{n+}-(NO)^{3-}$ . Note that the  $NO^{3-}$  group is isoelectronic to a peroxy ligand, both having four electrons in the  $\pi^*$  orbitals. Thus, the electron count for the metal–nitrosyl product in the spirit of the Enemark–Feltham notation should be  $(n+4)$ , and the complex should be denoted as  $\{M-NO\}^{n+4}$ . The nitride starting complex was denoted  $\{M-N\}^{n+4}$ . Taken all together, the “high-valent”  $\{Fe-N\}^8$  and the “low-valent”  $\{Fe-NO\}^8$ , presented here, are two of the same kind (for a more detailed reasoning of the electron count in  $\{Fe-N\}^8$  and  $\{Fe-NO\}^8$ ; see the SI and ref 63). Interestingly, the coordination chemist’s “eyeball” spectroscopy—based on the complex pair’s similar color—suggested related electronic structures, already.

## CONCLUSION

The reaction of the coordinatively unsaturated ferrous precursor  $[(TIMEN^{Mes})Fe](BF_4)_2$  (**1**) with nitrosonium tetrafluoroborate ( $NOBF_4$ ) yielded the diamagnetic  $\{Fe-NO\}^6$  species  $[(TIMEN^{Mes})Fe(NO)(CH_3CN)](BF_4)_3$  (**1**), the first member of a pentad of closely related nitrosyl complexes. Compound **1** revealed four redox transitions in the cyclic, linear-sweep, and square-wave voltammogram, centered between +0.32 and  $-3.45$  V vs  $Fe(Cp)_2^{+/0}$ . Chemical reduction by Zn, Mg, and Na/Hg, respectively, provided the isostructural trigonal, high-spin iron nitrosyl  $\{Fe-NO\}^{7,8,9}$  complexes,  $[(TIMEN^{Mes})Fe(NO)](BF_4)_x$  ( $x = 2$  (**2**),  $x = 1$  (**3**),  $x = 0$  (**4**)), and reduction of  $\{Fe-NO\}^9$  with cesium electride yielded a highly reduced  $\{Fe-NO\}^{10}$  fleeting intermediate that is a precursor to the nitrosoalkane derivative  $[Cs(\text{crypt-222})][(TIMEN^{Mes})Fe(NO)]$  (**5**), featuring a metalacyclic  $(NO-NHC)^{3-}$  moiety. These complexes render a new and the most complete series of low-valent iron nitrosyl complexes reported so far. They were fully characterized by single-crystal X-ray diffraction analysis (**1–4**), UV–vis electronic absorption, vibrational, multinuclear NMR, dual-mode EPR, and multifield-variable-temperature  $^{57}Fe$  Mössbauer spectroscopy and SQUID magnetization measurements. The obtained data offer a unique possibility to explore the molecular and electronic structures throughout the series in great detail, which—a priori—is extremely challenging because of the noninnocent nature of the ubiquitous NO ligand that can exist in up to five different oxidation and various spin states. Additionally, coordination of the NO ligand to the open-shell iron center can lead to a variety of molecular spin ground states. However, within this study, spectroscopy-based DFT calculations successfully reproduced all spectroscopic parameters and allowed for comprehensive interpretations and rational assignments of local oxidation and spin states for iron and the nitrosyl ligands of all compounds (**1–5**). The spectroscopic characterization, supplemented with the DFT computational analyses, revealed a low-spin Fe(II) electronic ground state of diamagnetic **1**, with a linearly coordinated nitrosonium ( $NO^+$ ) ligand bound *trans* to the N-anchor of the meridionally coordinating tris-carbene chelate and an equatorial acetonitrile ligand completing the octahedral coordination sphere. The reduction of **1** to **2** is accompanied by a change of NO and Fe spin states; cf., from  $NO^+$  bound to

low-spin Fe(II) in **1** (total spin  $S_t = 0$ ) to a  $^3NO^-$  bound to an oxidized high-spin Fe(III) in **2** (total spin  $S_t = 3/2$ ). However, subsequent reductions are metal-centered, leading to Fe(II) and Fe(I) nitroxyl complexes **3** ( $S_t = 1$ ) and **4** ( $S_t = 1/2$ ), respectively. Complexes **1–4** possess linear  $\{Fe-NO\}$  units. The highly reactive diamagnetic **5** ( $S_t = 0$ ) was isolated in the solid state and spectroscopically fully characterized. DFT calculations confirmed this nitrosoalkane species to be a tetragonal low-spin compound with a unique metalacyclic  $[Fe^{II}-(NO-NHC)^{3-}]$  unit, formed by partial NO insertion into the  $Fe-C_{NHC}$  bond upon formation of the fleeting intermediate  $\{Fe-NO\}^{10}$  species.

The series of  $\{Fe-NO\}^{6-9}$  complexes **2–4**, the intermediate  $\{Fe-NO\}^{10}$ , and its subsequently formed nitrosoalkane **5** are unprecedented to date and allowed for a systematic and thorough investigation, thereby unveiling the detailed electronic structures of this exceptional series of Fe–NO species.

## ASSOCIATED CONTENT

### Supporting Information

The Supporting Information is available free of charge on the ACS Publications website at DOI: 10.1021/jacs.9b08053.

General considerations, experimental methods, and synthetic details. Further characterization data of the complexes (CHN combustion analyses,  $^1H/^{13}C/^{19}F/^{11}B$  NMR, IR vibrational, UV/vis/NIR electronic absorption, EPR and  $^{57}Fe$  Mössbauer spectroscopic data, SQUID magnetization analyses (PDF)

X-ray data for obtained compounds (CIF)

Computational and single-crystal X-ray crystallographic details (PDF)

### Accession Codes

CCDC 1891802–1891806 and CCDC 1913650 contain the supplementary crystallographic data for this paper. These data can be obtained free of charge via [www.ccdc.cam.ac.uk/data\\_request/cif](http://www.ccdc.cam.ac.uk/data_request/cif), or by emailing [data\\_request@ccdc.cam.ac.uk](mailto:data_request@ccdc.cam.ac.uk), or by contacting The Cambridge Crystallographic Data Centre, 12 Union Road, Cambridge CB2 1EZ, UK; fax: + 44 1223 336033.

## AUTHOR INFORMATION

### Corresponding Authors

\*karsten.meyer@fau.de

\*shengfa.ye@kofo.mpg.de

### ORCID

Martin Keilwerth: 0000-0002-8801-6888

Frank W. Heinemann: 0000-0002-9007-8404

Jörg Sutter: 0000-0002-2300-9126

Andreas Scheurer: 0000-0002-2858-9406

Huayi Fang: 0000-0002-8008-0383

Eckhard Bill: 0000-0001-9138-3964

Frank Neese: 0000-0003-4691-0547

Shengfa Ye: 0000-0001-9747-1412

Karsten Meyer: 0000-0002-7844-2998

### Present Address

<sup>†</sup>(H.F.) Department of Chemistry, Fudan University, Shanghai 200433, China.

### Notes

The authors declare no competing financial interest.

## ACKNOWLEDGMENTS

This paper is dedicated to our friend, colleague, and mentor Karl Wieghardt, in recognition of his many important and creative contributions to chemistry. The study was financially supported by the German Federal Ministry of Education and Research (BMBF Grant No. 03SF0502), the Deutsche Forschungsgemeinschaft (DFG ME 1754/8-1), the Friedrich-Alexander-University of Erlangen-Nürnberg (FAU), and the Max-Planck-Institutes (MPIs) for Chemical Energy Conversion and Coal Research, in particular the Joint Workspace of MPI-CEC and MPI-KOFO. K.M. acknowledges constructive discussions with Patrick Holland (Yale University) on the occasion of the EICC-IV, and with Jesper Bendix (University of Copenhagen).

## REFERENCES

- (1) Culotta, E.; Koshland, D. E., Jr. NO news are good news. *Science* **1992**, *258*, 1862–1865.
- (2) Ignarro, L. J. *Nitric Oxide: Biology and Pathobiology*, 2nd ed.; Academic Press: San Diego, 2010.
- (3) Kuypers, M. M. M.; Marchant, H. K.; Kartal, B. The microbial nitrogen-cycling network. *Nat. Rev. Microbiol.* **2018**, *16*, 263–276.
- (4) Speelman, A. L.; White, C. J.; Zhang, B.; Alp, E. E.; Zhao, J.; Hu, M.; Krebs, C.; Penner-Hahn, J.; Lehnert, N. Non-heme High-Spin {FeNO}(6–8) Complexes: One Ligand Platform Can Do It All. *J. Am. Chem. Soc.* **2018**, *140*, 11341–11359.
- (5) Kupper, C.; Rees, J. A.; Dechert, S.; DeBeer, S.; Meyer, F. Complete Series of {FeNO}8, {FeNO}7, and {FeNO}6 Complexes Stabilized by a Tetracarbene Macrocyclic. *J. Am. Chem. Soc.* **2016**, *138*, 7888–7898.
- (6) Chalkley, M. J.; Peters, J. C. A Triad of Highly Reduced, Linear Iron Nitrosyl Complexes: {FeNO}8–10. *Angew. Chem., Int. Ed.* **2016**, *55*, 11995–11998.
- (7) Mingos, D. M. P. *Struct. Bonding (Berlin)*; Springer Verlag: Berlin, 2013; Vol. 153/154.
- (8) Roncaroli, F.; Videla, M.; Slep, L. D.; Olabe, J. A. New features in the redox coordination chemistry of metal nitrosyls {M–NO+; M–NO; M–NO–(HNO)}. *Coord. Chem. Rev.* **2007**, *251*, 1903–1930.
- (9) Hendriks, J.; Oubrie, A.; Castresana, J.; Urbani, A.; Gemeinhardt, S.; Saraste, M. Nitric oxide reductases in bacteria. *Biochim. Biophys. Acta, Bioenerg.* **2000**, *1459*, 266–273.
- (10) Speelman, A. L.; Lehnert, N. Heme versus Non-Heme Iron-Nitroxyl {FeN(H)O}8 Complexes: Electronic Structure and Biologically Relevant Reactivity. *Acc. Chem. Res.* **2014**, *47*, 1106–1116.
- (11) Enemark, J. H.; Feltham, R. D. Principles of Structure, Bonding, and Reactivity for Metal Nitrosyl Complexes. *Coord. Chem. Rev.* **1974**, *13*, 339–406.
- (12) Doctorovich, F.; Bikiel, D.; Pellegrino, J.; Suárez, S. A.; Larsen, A.; Martí, M. A. Nitroxyl (azanone) trapping by metalloporphyrins. *Coord. Chem. Rev.* **2011**, *255*, 2764–2784.
- (13) Berto, T. C.; Speelman, A. L.; Zheng, S.; Lehnert, N. Mono- and dinuclear non-heme iron–nitrosyl complexes: Models for key intermediates in bacterial nitric oxide reductases. *Coord. Chem. Rev.* **2013**, *257*, 244–259.
- (14) Hauser, C.; Glaser, T.; Bill, E.; Weyhermüller, T.; Wieghardt, K. The Electronic Structures of an Isostructural Series of Octahedral Nitrosyliron Complexes. *J. Am. Chem. Soc.* **2000**, *122*, 4352–4365.
- (15) Serres, R. G.; Grapperhaus, C. A.; Bothe, E.; Bill, E.; Weyhermüller, T.; Neese, F.; Wieghardt, K. Structural, Spectroscopic, and Computational Study of an Octahedral, Non-Heme {Fe–NO}6–8 Series: [Fe(NO)(cyclam-ac)]2+ / +0. *J. Am. Chem. Soc.* **2004**, *126*, 5138–5153.
- (16) Fujisawa, K.; Soma, S.; Kurihara, H.; Ohta, A.; Dong, H. T.; Minakawa, Y.; Zhao, J.; Alp, E. E.; Hu, M. Y.; Lehnert, N. Stable Ferrous Mononitroxyl {FeNO}8 Complex with a Hindered Hydrotris(pyrazolyl)borate Coligand: Structure, Spectroscopic Characterization, and Reactivity Toward NO and O2. *Inorg. Chem.* **2019**, *58*, 4059–4062.
- (17) Connelly, N. G.; Geiger, W. E. Chemical Redox Agents for Organometallic Chemistry. *Chem. Rev.* **1996**, *96*, 877–910.
- (18) Issa, D.; Dye, J. L. Synthesis of Cesium 18-Crown-6: The First Single-Crystal Electride? *J. Am. Chem. Soc.* **1982**, *104*, 3781–3782.
- (19) Dye, J. L. Electrides: Ionic Salts with Electrons as the Anions. *Science* **1990**, *247*, 663–668.
- (20) Dye, J. L. Electrons as Anions. *Science* **2003**, *301*, 607–608.
- (21) Hu, X.; Meyer, K. New tripodal N-heterocyclic carbene chelators for small molecule activation. *J. Organomet. Chem.* **2005**, *690*, 5474–5484.
- (22) Crevier, T. J.; Lovell, S.; Mayer, J. M. Chalcogen Atom Transfer to a Metal Nitrido. The First Transition Metal Selenonitrosyl Complex. *J. Am. Chem. Soc.* **1998**, *120*, 6607–6608.
- (23) Vogel, C.; Heinemann, F. W.; Sutter, J.; Anthon, C.; Meyer, K. An iron nitride complex. *Angew. Chem., Int. Ed.* **2008**, *47*, 2681–2684.
- (24) Kropp, H.; Scheurer, A.; Heinemann, F. W.; Bendix, J.; Meyer, K. Coordination-induced spin-state change in manganese(V) complexes: the electronic structure of manganese(V) nitrides. *Inorg. Chem.* **2015**, *54*, 3562–3572.
- (25) Karplus, M. Vicinal Proton Coupling in Nuclear Magnetic Resonance. *J. Am. Chem. Soc.* **1963**, *85*, 2870–2871.
- (26) Hesse, M.; Meier, H.; Zeeh, B. *Spektroskopische Methoden in der organischen Chemie*, 7th ed.; Thieme-Verlag: Stuttgart, Germany, 2002.
- (27) Scheurer, A.; Maid, H.; Hampel, F.; Saalfrank, R. W.; Toupet, L.; Mosset, P.; Puchta, R.; van Eikema Hommes, N. J. R. Influence of the Conformation of Salen Complexes on the Stereochemistry of the Asymmetric Epoxidation of Olefins. *Eur. J. Org. Chem.* **2005**, *2005*, 2566–2574.
- (28) Speelman, A. L.; Zhang, B.; Krebs, C.; Lehnert, N. Structural and Spectroscopic Characterization of a High-Spin {FeNO}(6) Complex with an Iron(IV)-NO(–) Electronic Structure. *Angew. Chem., Int. Ed.* **2016**, *55*, 6685–6688.
- (29) Praneeth, V. K. K.; Paulat, F.; Berto, T. C.; DeBeer George, S.; Näther, C.; Sulok, C. D.; Lehnert, N. Electronic Structure of Six-Coordinate Iron(III)-Porphyrin NO Adducts: The Elusive Iron(III)-NO(radical) State and Its Influence on the Properties of These Complexes. *J. Am. Chem. Soc.* **2008**, *130*, 15288–15303.
- (30) Speelman, A. L.; Lehnert, N. Characterization of a high-spin non-heme {FeNO}(8) complex: implications for the reactivity of iron nitroxyl species in biology. *Angew. Chem., Int. Ed.* **2013**, *52*, 12283–12287.
- (31) Wyllie, G. R. A.; Scheidt, W. R. Solid-State Structures of Metalloporphyrin NOx Compounds. *Chem. Rev.* **2002**, *102*, 1067–1089.
- (32) McQuilken, A. C.; Ha, Y.; Sutherlin, K. D.; Siegler, M. A.; Hodgson, K. O.; Hedman, B.; Solomon, E. I.; Jameson, G. N.; Goldberg, D. P. Preparation of non-heme {FeNO}7 models of cysteine dioxygenase: sulfur versus nitrogen ligation and photorelease of nitric oxide. *J. Am. Chem. Soc.* **2013**, *135*, 14024–14027.
- (33) McCleverty, J. A. Chemistry of Nitric Oxide Relevant to Biology. *Chem. Rev.* **2004**, *104*, 403–418.
- (34) Kupper, C.; Schober, A.; Demeshko, S.; Bergner, M.; Meyer, F. An Exclusively Organometallic {FeNO}7 Complex with Tetracarbene Ligation and a Linear FeNO Unit. *Inorg. Chem.* **2015**, *54*, 3096–3098.
- (35) Atanasov, M.; Aravena, D.; Suturina, E.; Bill, E.; Maganas, D.; Neese, F. First principles approach to the electronic structure, magnetic anisotropy and spin relaxation in mononuclear 3d-transition metal single molecule magnets. *Coord. Chem. Rev.* **2015**, *289*–290, 177–214.
- (36) Ye, S.; Price, J. C.; Barr, E. W.; Green, M. T.; Bollinger, J. M.; Krebs, C.; Neese, F. Cryoreduction of the NO-Adduct of Taurine:α-Ketoglutarate Dioxygenase (TauD) Yields an Elusive {FeNO}8 Species. *J. Am. Chem. Soc.* **2010**, *132*, 4739–4751.
- (37) Abragam, A.; Bleaney, B. *Electron Paramagnetic Resonance of Transition Ions*; Oxford University Press: Oxford, 1970.

- (38) Hendrich, M. P.; Debrunner, P. G. Integer-spin electron paramagnetic resonance of iron proteins. *Biophys. J.* **1989**, *56*, 489–506.
- (39) Hagen, W. R. *Biomolecular EPR Spectroscopy*; CRC Press: Boca Raton, 2009.
- (40) Mabbs, F. E.; Collison, D. *Electron Paramagnetic Resonance of d Transition Metal Compounds*; Elsevier: Amsterdam, 1992; Vol. 16.
- (41) Krzystek, J.; Ozarowski, A.; Telsler, J. Multi-frequency, high-field EPR as a powerful tool to accurately determine zero-field splitting in high-spin transition metal coordination complexes. *Coord. Chem. Rev.* **2006**, *250*, 2308–2324.
- (42) Güttlich, P.; Bill, E.; Trautwein, A. X. *Mössbauer Spectroscopy and Transition Metal Chemistry*; Springer Verlag: Berlin, 2011.
- (43) Pretsch, E.; Bühlmann, P.; Badertscher, M. *Structure Determination of Organic Compounds - Tables of Spectral Data*, 4th ed.; Springer-Verlag: Berlin, 2009.
- (44) Hu, X.; Castro-Rodriguez, I.; Olsen, K.; Meyer, K. Group 11 Metal Complexes of N-Heterocyclic Carbene Ligands: Nature of the Metal-Carbene Bond. *Organometallics* **2004**, *23*, 755–764.
- (45) Neese, F. Prediction and interpretation of the 57Fe isomer shift in Mössbauer spectra by density functional theory. *Inorg. Chim. Acta* **2002**, *337*, 181–192.
- (46) Ye, S.; Bill, E.; Neese, F. Electronic Structures of the [Fe(N<sub>2</sub>)(SiPiPr<sub>3</sub>)]<sup>+1/0/-1</sup> Electron Transfer Series: A Counter-intuitive Correlation between Isomer Shifts and Oxidation States. *Inorg. Chem.* **2016**, *55*, 3468–3474.
- (47) Debrunner, P. G., Mössbauer Spectroscopy of Iron Porphyrins. In *Iron Porphyrins Part III*; Lever, A. B. P., Gray, H. B., Eds.; VCH: Weinheim, 1989; Vol. III, pp 137–234.
- (48) Evans, W. J.; Fang, M.; Bates, J. E.; Furche, F.; Ziller, J. W.; Kiesz, M. D.; Zink, J. I. Isolation of a radical dianion of nitrogen oxide (NO)<sup>(2-)</sup>. *Nat. Chem.* **2010**, *2*, 644–647.
- (49) Weiner, W. P.; Bergman, R. G. Kinetics and Mechanism of the Formation of Nitrosoalkane Complexes by Migratory Insertion of Coordinated Nitric Oxide into Cobalt-Carbon Bonds. *J. Am. Chem. Soc.* **1983**, *105*, 3922–3929.
- (50) Montenegro, A. C.; Amorebieta, V. T.; Slep, L. D.; Martin, D. F.; Roncaroli, F.; Murgida, D. H.; Bari, S. E.; Olabe, J. A. Three redox states of nitrosyl: NO<sup>+</sup>, NO<sup>\*</sup>, and NO<sup>-</sup>/HNO interconvert reversibly on the same pentacyanoferrate(II) platform. *Angew. Chem., Int. Ed.* **2009**, *48*, 4213–4216.
- (51) Pellegrino, J.; Bari, S. E.; Bikiel, D. E.; Doctorovich, F. Successful Stabilization of the Elusive Species {FeNO}<sub>8</sub> in a Heme Model. *J. Am. Chem. Soc.* **2010**, *132*, 989–995.
- (52) Hu, B.; Li, J. One Electron Makes Differences: From Heme {FeNO}(7) to {FeNO}(8). *Angew. Chem., Int. Ed.* **2015**, *54*, 10579–10582.
- (53) Zolnhofer, E. M.; Käß, M.; Khusniyarov, M. M.; Heinemann, F. W.; Maron, L.; van Gastel, M.; Bill, E.; Meyer, K. An Intermediate Cobalt(IV) Nitrido Complex and its N-Migratory Insertion Product. *J. Am. Chem. Soc.* **2014**, *136*, 15072–15078.
- (54) Käß, M.; Hohenberger, J.; Adelhardt, M.; Zolnhofer, E. M.; Mossin, S.; Heinemann, F. W.; Sutter, J.; Meyer, K. Synthesis and Characterization of Divalent Manganese, Iron, and Cobalt Complexes in Tripodal Phenolate/N-Heterocyclic Carbene Ligand Environments. *Inorg. Chem.* **2014**, *53*, 2460–2470.
- (55) Park, J.; Song, H.; Kim, Y.; Eun, B.; Kim, Y.; Bae, D.; Park, S.; Rhee, Y. M.; Kim, W. J.; Kim, K.; Lee, E. N-Heterocyclic Carbene Nitric Oxide Radicals. *J. Am. Chem. Soc.* **2015**, *137*, 4642–4645.
- (56) Abernethy, C. D.; Codd, G. M.; Spicer, M. D.; Taylor, M. K. A Highly Stable N-Heterocyclic Carbene Complex of Trichloro-oxovanadium(V) Displaying Novel Cl-Carbene Bonding Interactions. *J. Am. Chem. Soc.* **2003**, *125*, 1128–1129.
- (57) Cheng, J.; Wang, L.; Wang, P.; Deng, L. High-Oxidation-State 3d Metal (Ti–Cu) Complexes with N-Heterocyclic Carbene Ligation. *Chem. Rev.* **2018**, *118*, 9930–9987.
- (58) Williams, D. S.; Meyer, T. J.; White, P. S. Preparation of Osmium(II) Nitrosyls by Direct Oxidation of Osmium(VI) Nitrides. *J. Am. Chem. Soc.* **1995**, *117*, 823–824.
- (59) Pipes, D. W.; Bakir, M.; Vitols, S. E.; Hodgson, D. J.; Meyer, T. J. Reversible Interconversion between a Nitrido Complex of Os(VI) and an Ammino Complex of Osmium(II). *J. Am. Chem. Soc.* **1990**, *112*, 5507–5514.
- (60) Odom, A. L.; Cummins, C. C. Nitric Oxide Cleavage: Synthesis of Terminal Chromium(VI) Nitrido Complexes via Nitrosyl Deoxygenation. *J. Am. Chem. Soc.* **1995**, *117*, 6613–6614.
- (61) Bendix, J.; Meyer, K.; Weyhermüller, T.; Bill, E.; Metzler-Nolte, N.; Wieghardt, K. Nitridocyanometalates of CrV, MnV, and MnV. *Inorg. Chem.* **1998**, *37*, 1767–1775.
- (62) Hummel, P.; Winkler, J. R.; Gray, H. B. Electronic structures of tetragonal nitrido and nitrosyl metal complexes. *Theor. Chem. Acc.* **2008**, *119*, 35–38.
- (63) Chang, H.-C.; Lin, Y.-H.; Werlé, C.; Neese, F.; Lee, W.-Z.; Bill, E.; Ye, S. Conversion of a Fleeting Open-Shell Iron-Nitride to an Iron-Nitrosyl. *Angew. Chem., Int. Ed.* **2019**, DOI: 10.1002/anie.201908689.